

AN ABSTRACT OF THE THESIS OF

Chih-Lan Jasmine Chuang for the degree of Master of Science in Mechanical Engineering presented on May 1, 2012.

Title: Application of Digital Image Correlation in Material Parameter Estimation and Vibration Analysis of Carbon Fiber Composite and Aluminum Plates.

Abstract approved:

Belinda A. Batten and Roberto Albertani

Identifying material parameters in composite plates is a necessary first step in a variety of structural applications. For example, understanding the material parameters of carbon fiber composite is important in investigating sensor and actuator placement on micro-air-vehicle wings for control and wing morphing purposes. Knowing the material parameters can also help examine the health of composite structures and detect wear or defects. Traditional testing methods for finding material parameters such as stiffness and damping require multiple types of experiments such as tensile tests and shaker tests. These tests are not without complications. Methods such as tensile testing can be destructive to the test specimens while use of strain gages and accelerometers can be inappropriate due to the lightweight nature of the structures.

The proposed inverse problem testing methods using digital image correlation via high speed cameras can potentially eliminate the disadvantages of traditional methods as well as determine the required material parameters including stiffness and damping by conducting only one type of experiment. These material parameters include stiffness and damping for both isotropic and orthotropic materials, and ply angle layup specifically for carbon fiber materials. A finite element model based on the Kirchoff-Love thin plate theory is used to produce theoretical data for comparison with experimental data collected using digital image correlation. Shaker experiments are also carried out using digital image correlation to investigate the modal frequencies as validation of the results of the inverse problem.

We apply these techniques first to an aluminum plate for which material parameters are known to test the performance and efficiency of the method. We then apply the method to a composite plates to determine not only these parameters, but also the layup angle. The inverse problem successfully estimates the Young's modulus and damping for the aluminum material. In addition, the vibration analysis produces consistent resonance frequencies for the first two modes for both theoretical and experimental data. However, carbon fiber plates present challenges due to limitations of the Kirchoff-Love plate theory used as the underlining theoretical model for the finite element approximation used in the inverse problem, resulting in a persistent mismatch of resonance frequencies in experimental data.

© Copyright by Chih-Lan Jasmine Chuang
May 1, 2012
All Rights Reserved

Application of Digital Image Correlation in Material Parameter Estimation and
Vibration Analysis of Carbon Fiber Composite and Aluminum Plates

by
Chih-Lan Jasmine Chuang

A THESIS
submitted to
Oregon State University

in partial fulfillment of
the requirements for the
degree of
Master of Science

Presented May 1, 2012
Commencement June 2012

Master of Science thesis of Chih-Lan Jasmine Chuang presented on May 1, 2012.

APPROVED:

Major Professors, representing Mechanical Engineering

Head of the School of Mechanical, Industrial, and Manufacturing Engineering

Dean of the Graduate School

I understand that my thesis will become part of the permanent collection of Oregon State University libraries. My signature below authorizes release of my thesis to any reader upon request.

Chih-Lan Jasmine Chuang, Author

ACKNOWLEDGMENTS

I would like to thank Dr. Belinda Batten for providing me the opportunity to continue my studies as a graduate student at Oregon State University. I really appreciate your advice, funding, and freedom to explore my research topic. It was my pleasure to have the opportunity to be both a research as well as a teaching assistant throughout my career as a graduate student. Thank you for your patience and understandings while helping me with my research, I really appreciate it.

I would also like to express my sincere gratitude to Dr. Roberto Albertani. Thank you very much for giving me the opportunity to use all the equipment while providing insightful guidance for our research. I thoroughly enjoyed the hands-on experience conducting experiments. Thank you for always having your door open to answer any questions that I had.

I am not only grateful to have great advisers as a graduate student, I am also indebted to my graduate colleague Cody Ray. I have learned so much from you. This includes learning \LaTeX , fixing and writing MATLAB codes, learning Inkscape, and having great inputs for my research. I especially thank you for being so patient while answering my never ending questions.

Of course, I would like to acknowledge the support of my family and friends. Thank you all very much for your understandings in giving me time and space to accomplish this big goal in my life.

I also appreciate my committee members for volunteering their time and providing feedback.

TABLE OF CONTENTS

	<u>Page</u>
1 Introduction	1
2 Theoretical Background and Literature Review	4
2.1 Digital Image Correlation	4
2.2 Parameter Estimation via an Inverse Problem Approach	8
2.3 Modal Analysis	10
3 Methodology of Material Parameter Estimation	14
3.1 The Finite Element Model and Laminate Theory	14
3.2 Vibration Analysis of Driven-Base Testing	21
4 Materials, Experimental Setup, and Testing Procedures	25
4.1 Fabrication of Test Specimens	25
4.1.1 Aluminum Plates	26
4.1.2 Carbon Fiber Plates	27
4.2 Experimental Testing Procedures	31
4.2.1 Digital Image Correlation Equipment	32
4.2.2 Error Analysis of Out-of-Plane Displacements	34
4.2.3 Tensile Testing of Uni-directional Carbon Fiber	35
4.2.4 Data Collection for Inverse Problems	38
4.2.5 Data Collection for Vibration Analysis	40
5 Results	44
5.1 Error Analysis of Digital Image Correlation	44

TABLE OF CONTENTS (Continued)

	<u>Page</u>
5.2 Carbon Fiber Material Parameters from Tensile Testing	46
5.3 Inverse Problems for Aluminum Plates	50
5.4 Inverse Problems for Carbon Fiber Plates	53
5.5 Vibration Analysis of Aluminum Plates	54
5.6 Vibration Analysis of Carbon Fiber Plates	56
6 Conclusions and Future Work	61
Appendices	65
A Experimental Procedures in Tensile Testing	65

LIST OF FIGURES

<u>Figure</u>	<u>Page</u>
2.1 Illustration of relation between displaced and reference images. . . .	6
3.1 Moments reacted to force on an infinitesimal plate element.	15
3.2 Relationship between reference and principal axes.	17
3.3 Cantilevered plate with one clamped edge and three free edges. . . .	19
3.4 Visualization of the flow of inverse problem.	19
3.5 Illustration of the cross section for the driven-base shaker test. . . .	22
4.1 Machine jig with dowel pins to align aluminum testing plates for machining.	26
4.2 Illustration of preparation of carbon fiber layup for curing in the oven.	28
4.3 Ensuring the release cloth is laid up in the same direction.	28
4.4 Carbon fiber plate clamped down by steel jig during CNC machining.	30
4.5 Tensile test specimen bonded with aluminum tabs.	31
4.6 Wiring of sync in and sync out between two cameras with external trigger.	32
4.7 Illustration of image correlation data collection and process flow. . .	33
4.8 Measurement setup for micrometer.	34
4.9 Camera setup with tensile testing.	36
4.10 Extensometer clamped to test specimen.	36

LIST OF FIGURES (Continued)

<u>Figure</u>	<u>Page</u>
4.11 Setup of inverse problem data collection.	39
4.12 Example of coordinate transformation in Vic-3D.	40
4.13 Setup with speckled plate and attachment.	42
5.1 Displacement matching results for the center of aluminum plate. . .	51
5.2 Material parameter estimation for 6061 aluminum plate.	51
5.3 Residual of full field displacement.	52
5.4 An example of inconsistent displacement matching results.	53
5.5 FRFs of input and output displacement of the aluminum samples. .	55
5.6 Average FRF of input and output displacement of the aluminum samples.	56
5.7 FRFs of the three carbon fiber samples with zero degree angle. . . .	57
5.8 Average FRF of the zero degree carbon fiber samples.	58
5.9 Three FRFs of 15 degree angle carbon fiber plates.	59
5.10 Average FRF of 15 degree angle carbon fiber samples.	59
5.11 An example of the 15 degree carbon fiber plate in second mode. . .	60

LIST OF TABLES

<u>Table</u>	<u>Page</u>
4.1 Tensile test specimen angles and dimensions.	29
4.2 Sets of images captured by cameras for finding material parameters.	37
5.1 Comparison of displacement measured and calculated.	45
5.2 95% confidence interval calculated using T-distribution.	46
5.3 Parameter results obtained from extensometer and digital image correlation.	49

1 INTRODUCTION

With continuously improving technology and computational power, digital image correlation (DIC) has become a very popular non-contacting testing method in analyzing the mechanics of structures. Preparation for test specimens is straight forward and almost any solid materials can be used by applying aerosol spray paints. DIC is especially beneficial in field test applications as no additional instrumentation is needed and images can simply be captured using high speed cameras. For example, DIC setup can be used to monitor structures such as bridges and wind turbine blades. Applications using DIC include biological testing investigating the strain and movement in muscles and veins, gear stress analysis, impact of bullets, and other experiments where test specimens are visible during testing and their images can be captured by cameras. Utilizing high speed cameras with high resolution, this project incorporates DIC for estimation of material parameters for aluminum and carbon fiber plates.

Aeroelastic applications such as micro-air-vehicles (MAVs) and wind turbine blades utilize carbon fiber composites due to their advantages in lightweight, tailorable stiffness, and flexibility in manufacturing process. To apply model identification and optimization for controlling such structures, accurate material parameters are essential in predicting dynamic behavior. Also, sensors and actuators can be used on MAVs during flight to morph or change the shape of the wings. In order to select the right locations for sensors and actuators, obtaining accurate values for the material parameters, such as stiffness and damping are important. In addition to control applications, knowing material parameters are also important in inspecting the health of structure for detecting defects and predicting potential failures.

As an initial attempt, coupling DIC via high speed cameras in this project with an inverse problem approach can be helpful in investigating the material properties of carbon fiber composite structures. Before testing the composite plates, the material parameters for an aluminum plate will first be analyzed to evaluate the performance and efficiency of the method.

Traditional testing methods require multiple types of experiments to obtain each individual material parameter. Often the experiments require repeatedly testing samples with equipment that can potentially damage the specimens. With other non-contact testing methods such as using laser vibrometers, the testing equipment can be extremely expensive with a time consuming data collection process. With the proposed testing method, only one type of experiment is required and it eliminates the need of producing multiple test runs. The test can be done directly to the structure of interest without causing any damage to the test specimen or alteration to its material properties. With a non-contact testing method using DIC for estimating material parameters, periodic inspection and repairs can also be done to prevent structure of interest from failure.

Background and motivation for using DIC throughout this project will be covered while similar work with inverse problems and vibration analysis for material characterization will be reviewed in Chapter 2. Chapter 3 covers the methods and algorithms used for the inverse problem in parameter estimation while providing some basic laminate theory incorporated in the existing finite element model. For vibration analysis, the chapter also extends the original Frequency Response Functions (FRFs) using output displacement and input force to find the output vs. input displacement FRFs. Calculation methods used in finding the theoretical resonance frequencies using finite element models for later comparison with the

shaker test in vibration analysis will also be presented.

Selection of materials, fabrication of test specimens, and testing procedures and equipment are described in detail in Chapter 4 including ad hoc error analysis of DIC, since the high speed cameras are used extensively for data collection. The aluminum material used has well-known material parameters; however, the values for the carbon fiber's material parameters have not been widely tested nor are they easily accessible. Standard tensile testing with an Instron machine using both the extensometer and DIC is performed to determine these parameters. Data collection for inverse problems is then described along with the procedures used in vibration analysis. Finally, experimental results, discussions for the inverse problem, tensile testing, vibration analysis, conclusions and suggestions for future work will be discussed in Chapter 5 and 6 respectively.

2 THEORETICAL BACKGROUND AND LITERATURE REVIEW

In this chapter, main subjects related to this project are presented, starting with the background and literature review of a non-contact, full field displacement data collection method called DIC. A brief review of the inverse problem approach and applications used in solving engineering problems is then explored. Finally, to validate the material parameters obtained from the inverse problems results, the basics of modal analysis and development of receptance FRF are reviewed as bases for further equation manipulations for future work. The method could be an alternative method in verifying the damping found in the inverse problem approach.

2.1 Digital Image Correlation

Traditional methods in collecting data in experimental mechanics include using accelerometers, extensometers, laser vibrometers, and strain gages. In order to use the majority of these tools for testing, some form of contact or bonding to the test specimens is required. With small and lightweight test specimens such as thin aluminum and composite plates, the weight of this test equipment can greatly affect the characteristics of the materials during testing. For example, while implementing a shaker test to understand the dynamics of a structure, accelerometers are attached to the test specimen for output acceleration measurements. When the weight of the accelerometers are approximately one fifth of the test specimen's weight, the effective weight of this setup with added accelerometer is altered and the experimental results do not accurately represent the original test specimen.

This is called mass rolling effect, and can be a large disadvantage in using testing equipment that requires some contact with lightweight test specimens.

In contrast to temporary bonding used to attach an accelerometer, the installation of strain gages on test specimens is permanent. Intricate preparation in soldering, wiring, and bonding of the strain gages is required for obtaining accurate strain readings while the removal of a strain gage causes irreparable damage to a specimen that cannot be used after testing. Vibrometers can be beneficial in terms of achieving non-contacting measurements; however, vibrometers are extremely expensive and the scanning data collection process is time consuming. Other complications for traditional testing include inability for measurement while structures are in operating conditions, as well as duplicates of testing samples that are required since removal of original structure of interest is impossible. With difficulties in material characterization using standard testing methods, it is helpful to find and use innovative technology and methods in understanding and obtaining material characteristics.

With computers' increasing processing abilities and digital camera technology, various optically based non-contacting full field measurements can be used in material characterization of composites. According to Grediac, various non-contacting full field measurements for displacements include: speckle, speckle interferometry, geometric moire, moire interferometry, holographic interferometry, DIC, and grid method [1]. DIC has become a popular method for collecting full field strain and displacement data due to its simplicity in test specimen preparation and data collection. It was first developed in the 1980s at the University of South Carolina but has become more popular recently due to improvements in computer capability and digital cameras [2]. To prepare the test specimens, a layer of spray paint is

first applied to the specimen to create a background medium that will provide a high level of contrast with speckles applied on the area of interest. For three dimensional displacement measurements, two synchronized cameras are calibrated and used for image capturing. Sutton et al. explains the basic theory of DIC in [3,4]. By comparing the displaced and reference images (Figure 2.1), a predetermined subset image size will be used in matching the same gray level intensity variation between reference and target images [5,6].

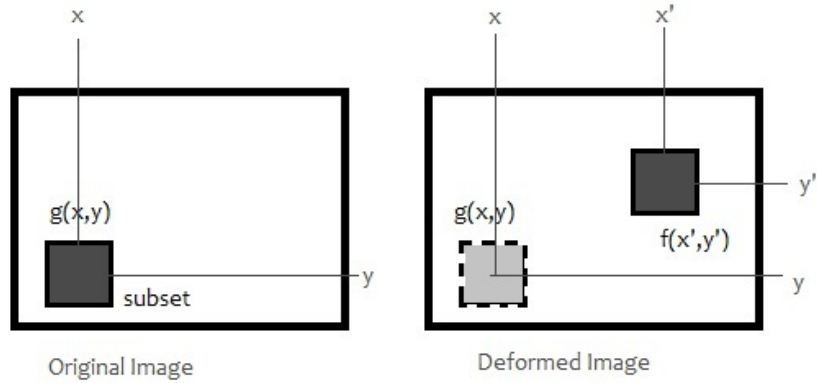


Figure 2.1: Illustration of relation between displaced and reference images.

In Figure 2.1, $g(x, y)$ and $f(x', y')$ are the gray intensity level at location, (x, y) and (x', y') respectively for reference and displaced images. The equation for calculating the correlation coefficient is [3, 5]:

$$K(a, b) = \frac{\sum_{i=1}^n \sum_{j=1}^n [g(x_i, y_i) - \bar{g}][f(x'_i, y'_i) - \bar{f}]}{\sqrt{\sum_{i=1}^n \sum_{j=1}^n [g(x_i, y_i) - \bar{g}]^2} \sqrt{\sum_{i=1}^n \sum_{j=1}^n [f(x'_i, y'_i) - \bar{f}]^2}}$$

where a and b are the displacements in the coordinate x and y directions and \bar{f} and \bar{g} are the average gray intensity of the reference and displaced locations. Having the displacements calculated, the strain can easily be found, if any.

With the use of synchronized high speed cameras, three-dimensional structural dynamics and vibration analysis can be examined and explored [7–9]. Although digital image correlation is becoming a popular technique for collecting full field displacement data, very little research has been done in conjunction with inverse problem approaches in determining material parameters. This project will expand the concepts and ideas similar to Nunes et al. [5, 10], where the image of a cantilevered aluminum beam in its first bending mode is captured and processed using DIC to determine its Young’s modulus. In addition to Young’s modulus, this project will expand the investigation to finding damping for both isotropic and an orthotropic material, as well as ply angle layup for orthotropic material.

Although DIC provides non-destructive advantages in inspection and testing, experiments have been done in exploring the measurement errors and possible causes [11–13]. Common uncertainty sources are calibration, camera angles, speckle size, image subset size, and lighting. With existing commercial software, a basic understanding of error analysis for the current experimental setup is essential. While DIC has its advantages in collecting data, it also has potential limitations. A balance between providing proper lighting during high speed image capturing while not overheating and changing the test specimen’s material properties is important. Proper selection of image subset size can eliminate unnecessary noise while obtaining accurate displacement data. Calibration and focus of camera should be carefully performed for the displacement range of the test specimen during testing.

2.2 Parameter Estimation via an Inverse Problem Approach

In general, parameter estimation is a type of inverse problem such that minimizing a cost function comprised of the difference between experimental and theoretical states, with respect to relevant parameters estimated. The parameters are estimated as “best-fit” of the theoretical model to available experimental data.

Inverse approaches contrast to direct problem approaches in which a model is used with known parameters such as Young’s modulus, density, or heat capacity to calculate the solutions analytically or numerically. Direct problem approaches usually are interested in the dependent variables that can be measured. For example, to find out the deflection of a cantilevered beam with a certain force applied to the free end, one can use the direct approach by specifying its boundary condition while plugging the known parameters such as Young’s modulus, the area moment of inertia of the beam, and the force applied to the known beam deflection equation. The challenge with a direct problem approach is that the “supposed known” parameters such as material parameters required are often unknown or cannot be easily obtained. Inverse problems utilize both the measured data as well as the theoretical model to extract these desired yet unknown parameters. For example, Nunes et al. utilize this inverse approach by finding the Young’s modulus based on the aluminum beam deflection measured by comparing the theoretical results from the beam deflection equation and measured results from DIC [5,10]. Any scientific problem that can be modeled analytically and for which experimental data can be calculated is suitable for the methodology of inverse problems [14–17].

Different mathematical models have been used in implementing the inverse problems such as Gauss-Newton algorithm, Levenberg-Marquardt algorithm, and

Nelder-Mead algorithm [5, 10, 18]. With an initial guess for the material parameters, an iterative process of calculations is performed by fitting the experimental measurements to the existing model until minimal differences are reached. The finite element model can then provide parameters that best estimate the behavior of the real structure. In the Gauss-Newton algorithm, parameters of a known model are estimated by iterating and setting the Jacobian and Hessian of the residual matrices or the difference between theoretical and experimental results to zero. The Levenberg-Marquardt algorithm uses similar technique as Gauss-Newton, yet it increments toward the greatest downward slope in finding minimal error between experimental and theoretical results.

In contrast to finding the steepest slope in searching for the minimum, the Nelder-Mead method forms a simplex with dimensions that match parameters to be estimated. A simplex of dimension n forms $n + 1$ vertices. For example, for a two dimensional simplex, it forms a triangle with three vertices. The initial simplex has to be nondegenerate such that its dimension points cannot be in the same hyperplane. It is a direct search method that requires no calculation of numerical or analytic gradients. The Nelder-Mead algorithm starts with an initial estimate which can be specified by the user and finds the minimum of a scalar function of variables [19]. The variables consist of the difference between finite element results and experimental results. The iterative process moves towards the decreasing values at the simplex's vertices and rejects the worst or greatest value of vertex and replaces it with the new found minimal vertex. The aim is to minimize the size of the simplex for minimal error or residual between finite element and measured results. It is a computationally intensive technique that requires reasonable initial guesses. However, due to its simplicity in implementation, Nelder-Mead is widely

used for inverse problem and parameter identification. Since the Nelder-Mead method does not require computing derivatives, it is helpful in dealing with data that contains noise as well as dealing with functions that are not smooth [20], which is why it is chosen as the algorithm used for parameter estimation for this project.

2.3 Modal Analysis

Modal analysis has been used to examine the behavior of structures under a certain excitation force to better understand their dynamic characteristics. Modal analysis can be extremely helpful in predicting structural behaviors, trouble-shooting vibration problems, testing for health and quality of a product, and designing and enhancing products to reduce overall vibrations. One focus of the modal analysis is to determine the damping parameters of the structure and the effect of the resonance frequencies which brings more information to material characterization. Damping of carbon fiber has been reviewed in [21] for micromechanical, macromechanical, as well as viscoelastic properties. In particular for the macromechanical approach, Adams et al. explains that during vibration, the structure's total energy lost can be treated as the superposition of energy lost due to stress in longitudinal, transverse, and shear direction [22, 23]. A Frequency Response Function (FRF) is a measure of an output response in frequency domain in comparison to an input stimulus. It is one common way in analyzing the output displacement, velocity, or acceleration of the structure due to a certain input force [24].

The change in damping parameters can effectively change the frequency response of the structure. In particular, the stiffness of a composite structure changes

with the layup and fiber orientation, hence the resonance frequency of the composite structure changes. Once the input force and output displacement, velocity, or acceleration are measured, the receptance, mobility, and accelerance FRFs can be calculated. Curve fitting to the experimental FRFs can be done to obtain the mass and damping parameters with known input force [24,25]. However, when the force applied to the lightweight structure cannot be obtained, driven-base modal testing should be done [26–28].

To validate driven-base modal testing, Carne compared the modal frequencies of an electronic package using both fixed-base and driving-base modal testing [26]. The results were comparable between driven-base and fixed-base testing with less than two percent of differences between the two methods. The remainder of this chapter will review the basics in obtaining naturally damped frequencies as well as receptance FRF covered in standard modal analysis text [24,25,29], which will be used in developing output and input displacement FRFs discussed in later chapter.

To obtain the receptance FRF, the matrix form of the equation of free vibration motion for multiple degrees of freedom can be written as:

$$M\ddot{x}(t) + C\dot{x}(t) + Kx(t) = 0 \quad (2.1)$$

where M , C , and K are the mass, damping, and stiffness matrix respectively. The vector x is in \mathbb{R}^n , where n is the degree of freedom specified by the user. By assuming Rayleigh proportional damping:

$$C = \alpha M + \beta K \quad (2.2)$$

such that damping matrix C is the superposition of mass and stiffness matrix M

and K with α and β as some damping constant coefficients, the rewritten equation

$$M\ddot{x}(t) + (\alpha M + \beta K)\dot{x}(t) + Kx(t) = 0 \quad (2.3)$$

can be used to diagonalize and decouple all of the mass and stiffness matrices such that each row in the matrix will represent one single mode shape of the structure. The mode shape matrix Ψ is first calculated, which contains the eigenvectors of the problem that will help simplify the matrix equation shown in Equation 2.3. Notice similar to a regular eigenvalues and eigenvectors problem, these eigenvectors are not unique hence the unique modal mass matrix, modal stiffness matrix, and mass-normalized mode shape need to be calculated. The unique modal mass matrix m_r is found by multiplying the mass matrix by the mode shape and its transpose:

$$m_r = \Psi^T M \Psi. \quad (2.4)$$

The modal stiffness matrix k_r is found by a similar concept in manipulating the original stiffness matrix:

$$k_r = \Psi^T K \Psi. \quad (2.5)$$

And the unique mass-normalized mode shape Φ is found:

$$\Phi = m_r^{-\frac{1}{2}} \Psi. \quad (2.6)$$

With unique mass-normalized mode shape Φ , the mass matrix M can be conveniently converted into an identity matrix:

$$\Phi^T M \Phi = I. \quad (2.7)$$

With all the matrices diagonalized and decoupled, each row derived from Equation 2.1 now represents the vibration motion for each mode of the structure. The natural frequency for a damped structure ω_{nd} can be represented as:

$$\omega_{nd} = \omega_r \sqrt{1 - \left(\frac{\alpha}{2\omega_r} + \frac{\beta\omega_r}{2}\right)^2}, \quad (2.8)$$

where ω_r is the natural frequency of the undamped structure, and is given by

$$diag(\omega_r^2)_{r=1}^n = \Phi^T K \Phi, \quad (2.9)$$

which is obtained similar to converting the mass matrix M to an identity matrix I . The FRF of a multiple degree of freedom structure η with proportional damping can be presented as:

$$\zeta_{ij}(\omega) = \sum_{r=1}^n \frac{\phi_{ir}\phi_{jr}}{\omega_r^2 - \omega^2}, \quad (2.10)$$

where ϕ_{ir} and ϕ_{jr} are the elements of mass-normalized mode shape matrix $[\Phi]$ presented in Equation 2.6 in column i and row j for each mode r . With proportional damping presented in Equation 2.2, α determines the viscous damping variation with respect to the mass of the structure such as air resistance and β is treated as an internal damping of the structure, also known as Kelvin-Voigt damping coefficient. With known input force and output displacements, methods such as peak-picking, circle-fit, and rational fraction polynomials can be used in finding the damping characteristics of material undergoing vibration analysis using FRF presented in Equation 2.10. The development of equations presented above will be used in expanding vibration analysis using input and output displacement instead of input force and output displacement.

3 METHODOLOGY OF MATERIAL PARAMETER ESTIMATION

This chapter will explain how an inverse problem approach is used in matching experimental results from DIC and theoretical results from an existing thin-plate finite element model. The thin plate model developed was originally used for investigating isotropic material such as aluminum plates. To explore the characteristics of uni-directional carbon fiber, the elastic behavior will be discussed for better understanding of the thin-plate finite element model used. For vibration analysis, some exploration of equations of FRF for input and output displacement will be presented in this chapter based on the original modal analysis presented in Chapter 2.3.

3.1 The Finite Element Model and Laminate Theory

The finite element model used in this project is based on linear Kirchhoff-Love plate theory [30], which includes assumptions such as the width and length of the plate are much greater than the thickness, the thickness of the plate is uniform during deformation, and there are no stresses perpendicular to the middle plane of the plate. The dynamic equation of the plate can be expressed as:

$$\rho h w_{tt} - \alpha w_t - (M_x)_{xx} - (M_y)_{yy} - (M_{xy})_{yx} - (M_{yx})_{xy} = f_n(t) \quad (3.1)$$

with $M_{xy} = M_{yx}$. In Equation 3.1, ρ is the density of the plate, h is the thickness of the plate, w is the out-of-plane displacement of the plate, M_x , M_y , and M_{xy} are the moments induced from the external force f_n applied to the plate shown in

Figure 3.1.

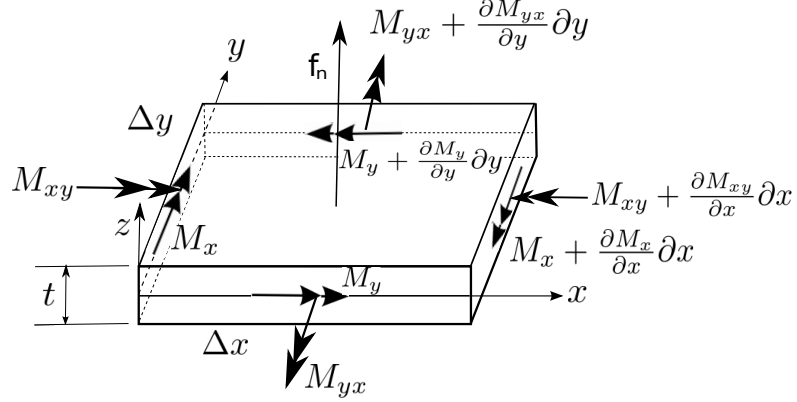


Figure 3.1: Moments reacted to force on an infinitesimal plate element.

In particular for each ply of carbon fiber k , the normal strains in x and y directions ϵ_x^k and ϵ_y^k as well as the shear strain γ_{xy}^k are found in basic elasticity theory as

$$\begin{aligned}\epsilon_x^k &= -z_k w_{xx} \\ \epsilon_y^k &= -z_k w_{yy} \\ \gamma_{xy}^k &= -2z_k w_{xy}.\end{aligned}\tag{3.2}$$

Adams et al. mentioned the changes in effect of the material property due to anisotropic layup of carbon fiber [22, 23, 31]. In general, different angle plies can be represented by a zero degree unidirectional carbon fiber ply with an angle transformation. For a detailed discussion of unidirectional carbon fiber's elastic behavior, see [32]. Unidirectional carbon fiber possesses the characteristics of an orthotropic material. With orthotropic materials, the material characteristics are uniform along three perpendicular directions. With the condition of having only in-plane stresses in x - y plane, the stress and strain relationship can be expressed

as

$$\begin{bmatrix} \sigma_1 \\ \sigma_2 \\ \tau_{12} \end{bmatrix} = \begin{bmatrix} Q_{11} & Q_{12} & 0 \\ Q_{12} & Q_{22} & 0 \\ 0 & 0 & Q_{66} \end{bmatrix} \begin{bmatrix} \epsilon_1 \\ \epsilon_2 \\ \gamma_{12} \end{bmatrix}, \quad (3.3)$$

where σ_1 and σ_2 are the normal stresses and τ_{12} is the shear stress in principal axes shown in Figure 3.2. Each Q_{ij} in Equation 3.3 is the reduced stiffness matrix component

$$Q_{ij} = C_{ij} - \frac{C_{i3}C_{j3}}{C_{33}} \quad (i, j = 1, 2, 6). \quad (3.4)$$

The stiffness matrix C is originally derived from the general anisotropic material's stress and strain relationship

$$\sigma = C\epsilon, \quad (3.5)$$

where σ is the 9×1 stress matrix, and ϵ is the 9×1 strain matrix. In particular,

$$Q_{11} = \frac{E_1}{1 - \nu_{12}\nu_{21}} \quad (3.6)$$

$$Q_{12} = \frac{\nu_{12}E_2}{1 - \nu_{12}\nu_{21}} \quad (3.7)$$

$$Q_{22} = \frac{E_2}{1 - \nu_{12}\nu_{21}} \quad (3.8)$$

$$Q_{66} = G_{12}, \quad (3.9)$$

where E_1 and E_2 are the Young's moduli along the principal axes, ν_{12} and ν_{21} are the Poisson's ratio while applying tension in each principal axis, and G_{12} is the shear modulus. The stress and strain relationship shown in Equation 3.4 is only valid when interested in directions parallel and perpendicular to the unidirectional carbon fiber.

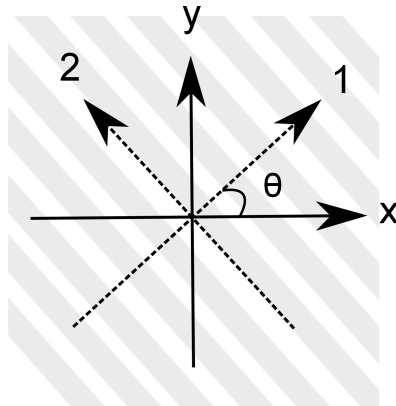


Figure 3.2: Relationship between reference and principal axes for unidirectional carbon fiber while looking down on a plate.

A transformation matrix T is used to realign the coordinate system from the principal axes to the reference coordinate system

$$T = \begin{bmatrix} m^2 & n^2 & 2mn \\ n^2 & m^2 & -2mn \\ -mn & mn & m^2 - n^2 \end{bmatrix} \quad (3.10)$$

where

$$m = \cos \theta \quad (3.11)$$

$$n = \sin \theta, \quad (3.12)$$

and θ is the angle of rotation of the carbon fiber with respect to the reference frame. The strain in the reference coordinate system can be obtained by multiplying the inverse of transformation matrix T to the strain in the principal axes

$$\begin{bmatrix} \epsilon_x \\ \epsilon_y \\ \frac{1}{2}\gamma_{xy} \end{bmatrix} = T^{-1} \begin{bmatrix} \epsilon_1 \\ \epsilon_2 \\ \frac{1}{2}\gamma_{12} \end{bmatrix}. \quad (3.13)$$

With the same concept, the stress components can also be realigned to the reference

frame

$$\begin{bmatrix} \sigma_x \\ \sigma_y \\ \frac{1}{2}\tau_{xy} \end{bmatrix} = T^{-1} \begin{bmatrix} \sigma_1 \\ \sigma_2 \\ \frac{1}{2}\tau_{12} \end{bmatrix}. \quad (3.14)$$

By applying the Kelvin-Voigt material model to Hooke's law, Equation 3.5 can be written as

$$\sigma = E\epsilon + \beta\epsilon_t \quad (3.15)$$

for a one dimension, purely axial load. In Equation 3.15, β is the same Kelvin-Voigt constant shown in Equation 2.2, which is proportional to the time derivative of strain ϵ , and E is the Young's modulus from the original Hooke's law. For the two dimensional case, Equation 3.15 can be rewritten as

$$\begin{aligned} \begin{bmatrix} \sigma_1 \\ \sigma_2 \\ \frac{1}{2}\tau_{12} \end{bmatrix} &= \frac{1}{1 - \nu_{12}\nu_{21}} \begin{bmatrix} E_1 & \nu_{21}E_1 & 0 \\ \nu_{12}E_2 & E_2 & 0 \\ 0 & 0 & G_{12}(1 - \nu_{12}\nu_{21}) \end{bmatrix} \begin{bmatrix} \epsilon_1 \\ \epsilon_2 \\ \frac{1}{2}\gamma_{12} \end{bmatrix} \\ &+ \frac{1}{1 - \nu_{12}\nu_{21}} \begin{bmatrix} \beta_1 & \nu_{21}\beta_1 & 0 \\ \nu_{12}\beta_2 & \beta_2 & 0 \\ 0 & 0 & \beta_{12}(1 - \nu_{12}\nu_{21}) \end{bmatrix} \begin{bmatrix} \epsilon_{1t} \\ \epsilon_{2t} \\ \frac{1}{2}\gamma_{12t} \end{bmatrix}. \end{aligned} \quad (3.16)$$

Equations 3.13 and 3.14 can be applied to transform Equation 3.16, which represents the stress and strain relationship for an orthotropic material with an assumption of Kelvin-Voigt damping in the reference coordinate system presented in Figure 3.2. Substituting the strains from Equation 3.2 into Equation 3.16 and integrating over the out-of-plane direction will give the theoretical displacement of the plate in the time domain using finite element model.

In the simulations, the finite element model uses a grid size of 6×24 for width and length, which has a length to width ratio of four. A cubic B-spline is used as the basis for the finite element approximation scheme. The degree of freedom n is specified by the total number of nodes used, which is 175 in this case. The

boundary condition can be specified with the bottom edge clamped as shown in Figure 3.3, while the rest of the three edges are free.

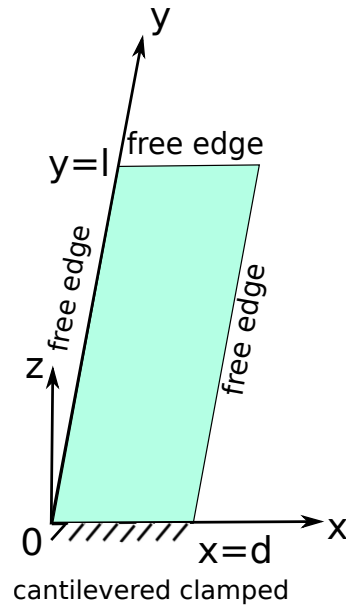


Figure 3.3: Cantilevered plate with one clamped edge and three free edges.

With an existing finite element code developed with cantilever boundary conditions for both the aluminum and carbon fiber plates as well as the data collected using DIC, an inverse problem is used in computing the difference between finite element and experimental data to estimate the material parameters. The general concept in estimating the material parameter is visualized in Figure 3.4.

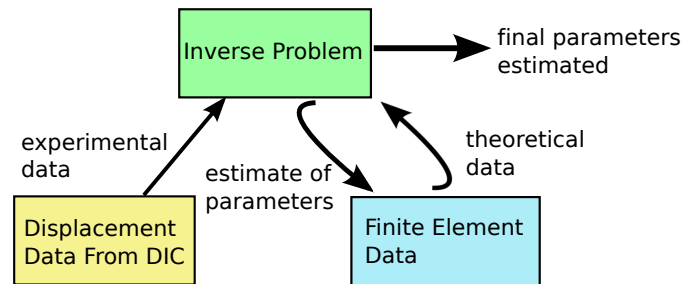


Figure 3.4: Visualization of the flow of inverse problem.

The inverse problem in this project utilizes Nelder-Mead algorithm due to its simplicity and capability in dealing with noisy data from experimental results [19]. As discussed in Chapter 2, it is a simplex based algorithm with dimensions matching the amount of parameters to be estimated. For estimating the model for the aluminum plates, the parameters include Young's modulus E and the damping parameters α and β . For estimating the model for the carbon fiber plates, the parameters include Young's modulus and Kelvin-Voigt damping in each direction E_1 , E_2 , β_1 , and β_2 , viscous damping similar to the aluminum plate α , and multiple plies of carbon fiber orientation θ .

The user assigns an initial guess for all the parameters as input for the finite element model. The finite element model then computes the theoretical results for the plate's displacement in the time domain and feeds them back to the inverse problem. A comparison using L_2 norm is done to calculate the residual error between the experimental data and the finite element results:

$$residual = \sqrt{\sum_{i=1}^N (w_i(t) - f_i(t))^2}, \quad (3.17)$$

where $w_i(t)$ and $f_i(t)$ denote the experimental and finite element displacement data in time domain at each node i over the entire plate with 7×25 total nodes. As presented in Figure 3.4, the curved arrows show an iterative process being utilized in searching for the minimal residual value in Equation 3.17 between data from DIC and finite element calculation. The estimated parameters yield results that can then be treated as the material parameters characterized.

3.2 Vibration Analysis of Driven-Base Testing

Similar to driven-base modal testing done by Carne that uses input and output acceleration to obtain a FRF [26], input and output displacements will be used in finding resonance frequencies for the first couple modes. With standard modal analysis covered by He and Fu [24], in addition to Carne's fundamental equations developments following [24, 26, 28], this section will cover the development of equations for motion to motion vibration analysis using displacements. The goal in developing this output vs. input displacement FRF is to have a theoretical representation of the FRF obtained from shaker testing. FRFs obtained from multiple sets of experiment can be conveniently averaged directly in the frequency domain. In addition, the process in finding the resonance frequency using the parameters estimated from the inverse problem will be discussed for comparison with resonance frequency obtained from the shaker test.

The free vibration equation will start in the same form presented in [26]:

$$M(\ddot{u} + \ddot{u}_0) + C(\dot{u} + \dot{u}_0) + K(u + u_0) = 0, \quad (3.18)$$

where M , C , and K are the mass, damping, and stiffness matrices, respectively. u_0 is the rigid body of input base displacement and u is the output displacement, also known as the elastic displacement with respect to u_0 of the structure. Figure 3.5 shows the cross section of a cantilevered plate clamped at the base of the plate and excited by a shaker.

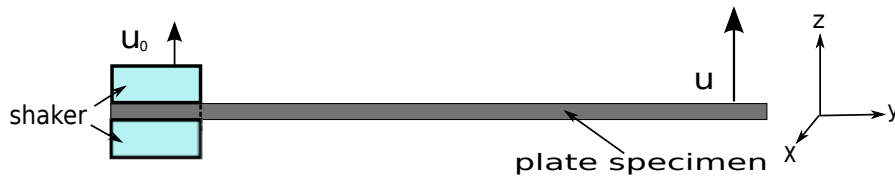


Figure 3.5: Illustration of the cross section for the driven-base shaker test of a cantilevered plate with input and output displacement.

Both u_0 and u shown in Figure 3.5 are the displacements in the time domain and can be recorded by digital image correlation via a pair of synchronized high speed cameras. By applying proportional damping discussed previously ($C = \alpha M + \beta K$) in addition to the assumption of rigid body motion of the input base $Ku_0 = 0$ and $Cu_0 = 0$, Equation 3.18 becomes:

$$M\ddot{u} + (\alpha M + \beta K)\dot{u} + Ku = -M\ddot{u}_0. \quad (3.19)$$

To uncouple the mass and stiffness matrices in Equation 3.19, the unique mass-normalized matrix Φ and its transpose will be multiplied to Equation 3.19 to get

$$\Phi^T M \Phi \ddot{u} + (\alpha \Phi^T M \Phi + \beta \Phi^T K \Phi) \dot{u} + \Phi^T K \Phi u = -\Phi^T M \Phi \ddot{u}_0. \quad (3.20)$$

As mentioned in standard modal analysis covered in Chapter 3, $\Phi^T M \Phi$ equals to the identity matrix I and $\Phi^T K \Phi$ equals $diag(\omega_r^2)_{r=1}^n$ where ω_r in each row of the matrix is the resonance frequency for each mode. Equation 3.20 can then be rewritten as

$$I\ddot{u} + (\alpha I + \beta \omega_r^2)\dot{u} + \omega_r^2 u = -I\ddot{u}_0. \quad (3.21)$$

Representing Equation 3.21 in the frequency domain by taking the Fourier transform will allow one to eventually obtain the FRF of input and output displacement.

After the Fourier transform, Equation 3.21 in the frequency domain now has the form

$$-I\omega^2 U + (\alpha I + \beta\omega_r^2)i\omega U + \omega_r^2 U = I\omega^2 U_0, \quad (3.22)$$

where U and U_0 are the elastic output displacement and rigid input displacement of the structure in the frequency domain. The frequency response function for total output displacement $U + U_0$ and input displacement U_0 can be written as:

$$\frac{U + U_0}{U_0} = (I\omega^2 + I)(-I\omega^2 + i\omega(\alpha I + \beta\omega_r^2) + \omega_r^2)^{-1} \quad (3.23)$$

To normalize Equation 3.23, a mass-normalized mode shape matrix is used to obtain the FRF $\Gamma(\omega)$ in the frequency domain ω :

$$\Gamma(\omega) = \Phi((I\omega^2 + I)(-I\omega^2 + i\omega(\alpha I + \beta\omega_r^2) + \omega_r^2)^{-1})\Phi^T \quad (3.24)$$

Equation 3.24 is the representation of the output vs. input FRF, which should be the theoretical representation of FRFs obtained from the shaker test. The damping parameters α and β can potentially be extracted from the experimental data using Equation 3.24 as verification for the inverse problem.

As an alternative in verifying the damping parameters, the theoretical resonance frequency can also be calculated using the material parameters estimated from the inverse problem. From Equation 3.19, it can be rewritten in the form of ordinary differential equation by substituting u and \dot{u} as

$$\begin{aligned} h_1 &= u \\ h_2 &= \dot{h}_1 = \dot{u} \end{aligned}$$

to get

$$\begin{bmatrix} \dot{h}_1 \\ \dot{h}_2 \end{bmatrix} = \begin{bmatrix} 0 & 1 \\ -KM^{-1} & -CM^{-1} \end{bmatrix} \begin{bmatrix} h_1 \\ h_2 \end{bmatrix} + \begin{bmatrix} 0 \\ -\ddot{u}_0 \end{bmatrix}. \quad (3.25)$$

Equation 3.25 has the form of

$$\dot{h} = Ah + B, \quad (3.26)$$

such that

$$A = \begin{bmatrix} 0 & 1 \\ -KM^{-1} & -CM^{-1} \end{bmatrix} \quad (3.27)$$

and

$$B = \begin{bmatrix} 0 \\ -\ddot{u}_0 \end{bmatrix}. \quad (3.28)$$

And by finding and sorting the eigenvalues ω_r for each mode r of matrix A from the lowest value, the resonance frequencies for the first few modes f_r can be obtained

$$f_r = \frac{\omega_r}{2\pi}. \quad (3.29)$$

Now having a basic understanding of the methodology used for the inverse problem approach and vibration analysis, various experiments will be performed in attempt to estimate the material parameters and verifying them by comparing the resonance frequencies. The next chapter will describe the materials used, experimental setup, as well as the test procedures used in conducting various testings.

4 MATERIALS, EXPERIMENTAL SETUP, AND TESTING PROCEDURES

This chapter will first explain the reasons of material selection for test specimens. Once the material is selected and obtained, the procedures in fabricating and machining the test specimens in order to obtain consistent test pieces will be covered. Digital image correlation is used in both inverse problem and vibration analysis data collection, hence the equipment setup will then be described. The setups for both inverse problem and modal analysis will also be documented as a reference for validating or extending current works.

4.1 Fabrication of Test Specimens

In fabricating the test specimens, aluminum alloy and uni-directional carbon fiber materials are used. Aluminum is chosen due to its known isotropic material properties. Isotropic materials such as aluminum have uniform Young's modulus. On the other hand, uni-directional carbon fiber is chosen due to its anisotropic material property which allows freedom in tailoring the material parameters. Unlike isotropic materials, anisotropic materials such as unidirectional carbon fiber have various Young's moduli. In particular, for unidirectional carbon fiber, the material parameters are uniformed in two orthogonal directions: along the unidirectional fiber and in-plane perpendicular to the unidirectional fiber. This specific case of an anisotropic material property is also described as an orthotropic material. While expressing the stiffness matrix for unidirectional carbon fiber, the independent components are reduced from an anisotropic material of 36 variables to 9 vari-

ables total. Carbon fiber laminates with different mechanical characteristics can be constructed by laying up plies in different fiber orientations.

The following sections will explain the procedures used in constructing the test specimens and obtaining the desired testing dimensions.

4.1.1 *Aluminum Plates*

The aluminum test specimens are aluminum alloy 6061. The material comes in 1.5m² sheet with 0.78mm in thickness. A sheet metal break is first used to cut the material into approximate dimension with 0–5mm tolerance. To ensure consistent dimensions desired for all aluminum plates, these plates are stacked and placed into a jig with dowel pins for accurate alignment and trimmed with an end mill on all four sides.

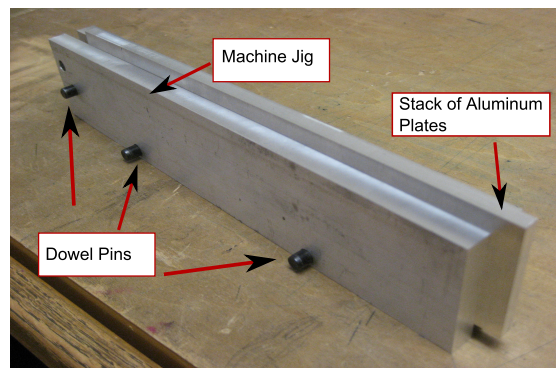


Figure 4.1: Machine jig with dowel pins to align aluminum testing plates for machining.

The final aluminum test specimens are 48.22mm × 229.0mm × 0.78mm in width, length, and thickness, respectively. When the test specimens are clamped in both the vice and the shaker's fixture for inverse and vibration data collection, the cantilever plates have a four to one ratio, length to width with a deviation of

0.8%. An aspect ratio of four allows the inverse problem to easily compare data between experimental and finite element results, as finite element convergence is expedited by using square elements.

4.1.2 Carbon Fiber Plates

The material used in the carbon fiber test specimens is pre-impregnated Toray T800 unidirectional carbon fiber. Two types of composite plates are constructed each with four plies of unidirectional carbon fiber. An even number of carbon fiber layers is chosen for ease of finite element modeling for theoretical data. The carbon fiber plate will have a symmetric layup. With an even number of layers, the mid-plane of the carbon fiber plate will be evenly divided and in between two middle layers of carbon fiber instead of having the middle carbon fiber layer split in half. A thinner carbon fiber plate exhibits greater flexibility and displacement during testing. However, unidirectional carbon fiber plates with only one or two layers can easily be damaged during testing. Having four layers of carbon fiber provides a good balance between appropriate damping range as well as structural soundness for testing.

The first type of composite plate fabricated has uniform fiber direction close to zero degree angle along the length of the plate. The second type of composite plate has an uniform off-angle fiber orientation that is approximately 15° . Both types of carbon fiber plates are laid up and vacuum bagged as shown in Figure 4.2. The curing temperature cycle is operated specified by the manual specified from the carbon fiber manufacturing company Toray Inc.

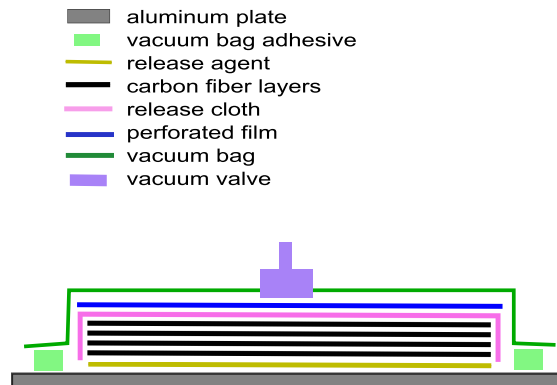


Figure 4.2: Illustration of preparation of carbon fiber layup for curing in the oven.

During the layup process, it is important to align the release cloth in the same direction as the carbon fiber plates. With misaligned release cloth, the fiber within the plate can be easily separated when peeling off the release cloth and the plate will be damaged. Once the carbon fiber plates are cured, each plate is machined down to the desired dimensions using an existing jig for consistency.

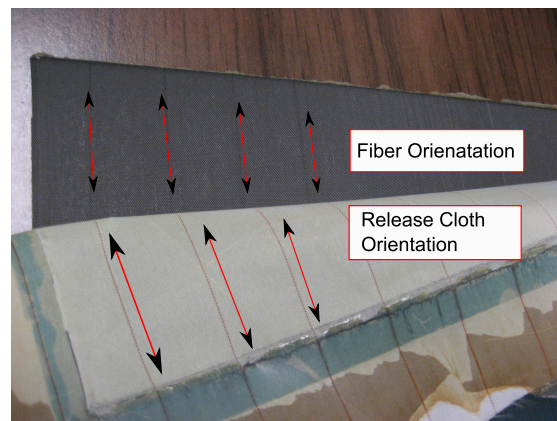


Figure 4.3: Ensuring the release cloth is laid up in the same direction as the carbon fiber plate can reduce damage to testing specimen.

The final dimensions of the carbon fiber plates are $48.38\text{mm} \times 228.70\text{mm} \times 0.96\text{mm}$ for width, length, and thickness, respectively. When the test specimens are clamped in both the vice and the fixture on a shaker for inverse and vibration

data collection, the cantilever plates have a ratio of four to one, length to width with a deviation of 0.6%.

In fabricating the carbon fiber test specimens for tensile test on an Instron machine, a similar process is done in laying up the carbon fiber material. The specimen geometry is shown in Table 4.1 based on ASTM testing standards [33] as well as the ten-degree off-axis test presented in [34]. According to the ASTM testing standards for carbon fiber tensile tests, specific width, length, and thickness are required for different testing specimens with different angle layups. Using the specific T800 unidirectional carbon fiber, the layers shown in Table 4.1 are able to achieve the desired thickness for each sample.

Table 4.1: Tensile test specimen angles and dimensions based on ASTM testing standards.

Fiber Orientation	Width (mm)	Length (mm)	thickness (mm)	Layers
0° unidirectional	15.0	250.0	1.0	5
90° unidirectional	25.0	175.0	2.0	10
10° unidirectional	15.0	250.0	1.0	5

The same steel jig is used in clamping the carbon fiber material while it is being trimmed using a CNC machine shown in Figure 4.4. A carbide end mill of $\frac{5}{16}$ inch (7.93mm) in diameter is used in cutting the carbon fiber plate.



Figure 4.4: Carbon fiber plate clamped down by steel jig during CNC machining.

In order to preserve and extend the life of the cutter as well as having consistently clean edges on testing samples, a ramp down motion is programmed into the CNC machine to utilize the whole length of the cutter instead of repeatedly using the same range of the cutter that is the thickness of the plate. A spray water bottle is used during machining to reduce carbon dust in the air. As seen in Figure 4.4, the jig can be used for cutting samples for different sample sizes as well as the actual testing plate for inverse problem and vibration analysis.

Referencing the testing standard presented in [33], machined aluminum bonding tabs are glued to the ends of all tensile test specimens shown in Figure 4.5 and cured in the oven using the cure cycle suggested.

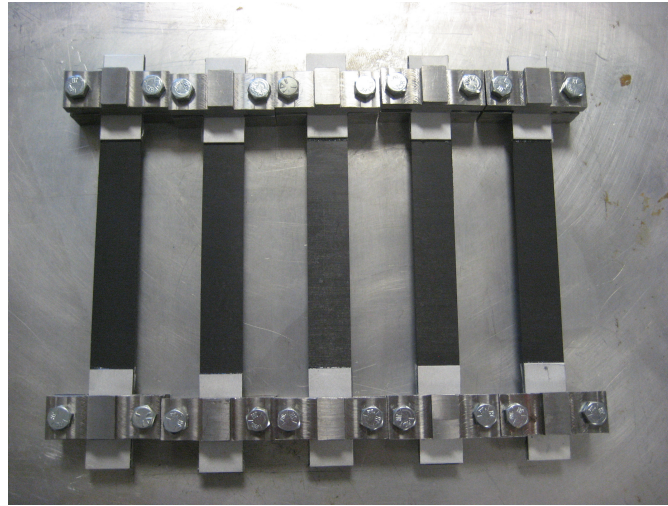


Figure 4.5: Tensile test specimen bonded with aluminum tabs.

4.2 Experimental Testing Procedures

To investigate the material characteristics of carbon fiber and aluminum plates, high speed cameras are used extensively throughout this project, hence an ad hoc error analysis experiment will first be presented to estimate the limitation of the cameras with current setup. The 6061 aluminum material used for testing has well known material parameters; however, the T800 uni-directional carbon fiber does not have consistent known parameters listed. To have a material parameter datum for comparison with results from the inverse problem, traditional tensile test will be done on an Instron machine using both extensometer as well as DIC for recording carbon fiber test specimen's deformation. Finally, the test procedures for data collection for inverse problem as well as vibration analysis will be discussed for future experimental validation or expansion based on this project.

4.2.1 Digital Image Correlation Equipment

The two high speed cameras used for DIC setup are S-PRiplus cameras from AOS Technologies AG. They are capable of capturing images at as high as 1250 frame per second with basic resolution of 800×600 pixel with a shutter speed of 500ms. With highest resolution of 1280×1024 pixel, the cameras are able to record images at 500 frame per second. The camera lenses used with the high speed cameras are AF Zoom-Nikkor by Nikon with focal length of 24-85mm and a fast f/2.8 maximum aperture.

With the test specimens machined to the desired dimensions, the plates are first prepared with an even layer of flat white spray paint. Once the paint is dried, a black speckle pattern is then applied by aerosol. During high speed image capturing, two 250 Watt lamps are used to ensure the brightness of the images captured. In order to have both high speed cameras capturing images with frame synchronization, a hardwire connection is needed for the synchronized-in wire of the first camera and synchronized-out wire of the second camera. When the cameras are set up as shown in Figure 4.6, camera one with the synchronized-out connection will be treated as the master camera while the second camera will be the slave camera. The trigger will be connected to the master camera to activate image capturing.

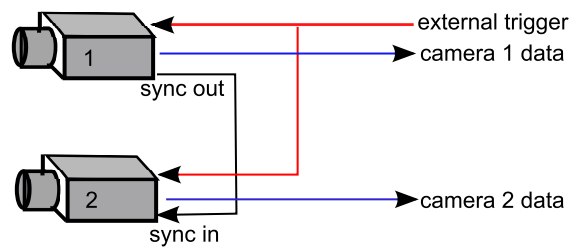


Figure 4.6: Wiring of sync in and sync out between two cameras with external trigger.

AOS Imaging Studio V3 is the software used in adjusting the settings for camera properties as well as monitoring the overall camera setup before data collection. Since this project requires both cameras to have synchronized settings with identical frame rate, the global command is activated in AOS Imaging Studio. Before image files are processed by the commercial software Vic-3D to calculate strain and displacement data, a software called ReNamer is used to adjust all image file names and make them suitable for Vic-3D. A series of calibration images are taken on a known dimension grid in order to calculate the camera orientations and correctly process the images captured during testing. Once Vic-3D has processed the output data images, computing programs such as MATLAB is used for processing the iterations of the inverse problem and producing FRFs in vibration analysis. The overall processing of DIC is illustrated in Figure 4.7, such that both calibration images with blue arrows and experimental images with red arrows captured by the cameras are first processed through the ReNamer for consistent file names. The calibration images are first used in Vic-3D to properly setup the right calibration in order to process experimental images. Only the results of the experimental images obtained from Vic-3D are then passed down to MATLAB to apply the inverse problem in finding displacement or resonance frequencies.

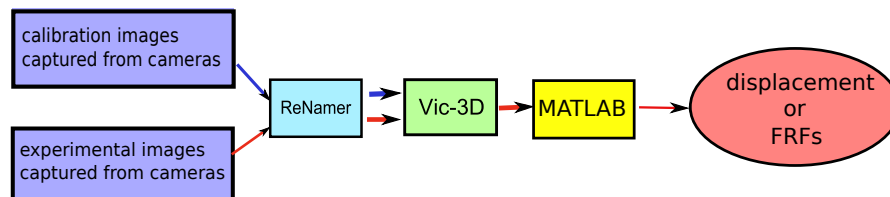


Figure 4.7: Illustration of image correlation data collection and process flow.

Now knowing the overall process of data collection using DIC, the next section will cover the test procedures used for the error analysis of out-of-plane displace-

ment in DIC.

4.2.2 Error Analysis of Out-of-Plane Displacements

The displacement uncertainty recorded by DIC can vary based on camera angles, speckle size, subset size, and lighting. Exploring each of the variables to analyze the errors is beyond the scope of this project; however, having an error analysis for the cameras with the current setup is important in estimating the experimental uncertainty. In both the inverse problem as well as vibration analysis, the out-of-plane displacement is the main focus of data acquisition.

An ad hoc experiment is performed to determine the accuracy of the camera resolution for out-of-plane displacement by comparing the known displacement from a micrometer with the data obtained from the commercial software Vic-3D. An aluminum testing plate with speckle pattern is placed on a Mitutoyo micrometer head secured by a fixture and a vice shown in Figure 4.8. The vice can be adjusted and rotated in all three axes to ensure the displacement is purely out of plane.



Figure 4.8: Measurement setup for micrometer and speckled plate specimen for out-of-plane displacement error analysis.

The overall setup is similar to the inverse problem and vibration analysis that will be explained in later sections except the plate is stationary and attached to a micrometer head. The Mitutoyo micrometer head used has a smallest increment of 0.01mm. Five sets of images are captured. The first set of images is recorded as a reference for zero displacement. With each revolution, the micrometer head displaces 0.5mm. The cameras capture a set of images per revolution from the micrometer, and the images are then processed using Vic-3D to calculate the out-of-plane displacement for comparison with the micrometer's measurement.

As mentioned previously, unlike the aluminum 6061, carbon fiber used throughout this project has not been widely tested and the material parameters are not consistently known. Next section will cover the tensile testing procedures for finding the Young's modulus, Poisson's ratio, and shear modulus specifically for the T800 carbon fiber material used based on ASTM standards.

4.2.3 Tensile Testing of Uni-directional Carbon Fiber

The purpose of this experiment is to obtain the material parameters for T800 uni-directional carbon fiber such as Young's moduli E_1 and E_2 , Poisson's ratios ν_1 and ν_2 , as well as shear modulus G . Although two high speed cameras are set up for the tensile data collection, only one camera is needed for two dimensional measurement. For determining Young's moduli and Poisson's ratios, five test samples are used for both 0° and 90° orientations. The width and thickness of each test specimen are measured at the top, middle, and the bottom position for averaging before the speckle pattern is applied. As shown in Figure 4.9, once the cameras are set up and calibrated, the first test specimen is used as a mock-up for evaluation of

the Instron machine inputs such as rate of data recording and machine operation, as well as finding the appropriate force applied by the machine as an indication to remove the extensometer.



Figure 4.9: Camera setup with tensile testing.

The extensometer shown in Figure 4.10 and the high speed cameras are used at the same time in collecting data for material parameters.

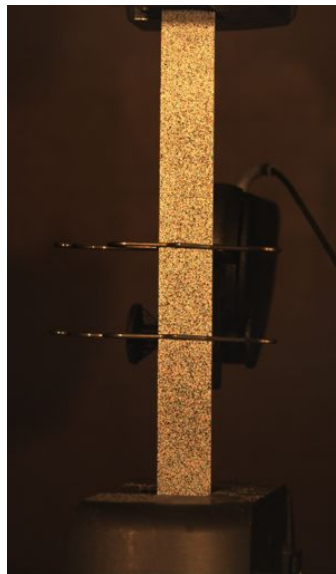


Figure 4.10: Extensometer clamped to test specimen while images are captured by high speed cameras.

Once the first specimen is broken while experiencing its ultimate tensile strength, the extensometer removal indication is set at half of the ultimate tensile strength to ensure no damage is done on the extensometer. With the ultimate tensile strength approximated from the first sample, the high speed cameras can then be set incrementally by activating multiple buffer settings to capture a series of images at each known force applied by the Instron machine. At each increment, 20 frames of images are taken at 20 frames per second. While the strain reading from the extensometer is zeroed and balanced, the first set of images are taken as reference images. After the initial set of images, 10 more sets of images are taken. Table 4.2 shows the force applied by the Instron machine when images are taken for different types of samples.

Table 4.2: Sets of images captured by synchronized cameras for determining material parameters.

set #	1	2	3	4	5	6
0 degree	0kN	4kN	8kN	12kN	16kN	20kN
90 degree	0kN	0.13kN	0.26kN	0.39kN	0.52kN	0.65kN
10 degree	0kN	0.35kN	0.70kN	1.05kN	1.40kN	1.75kN
set#	7	8	9	10	11	
0 degree	24kN	28kN	32kN	36kN	40kN	
90 degree	0.78kN	0.91kN	1.04kN	1.17kN	1.30kN	
10 degree	2.0kN	2.45kN	2.80kN	3.15kN	3.5kN	

Ten sets of images taken at various forces applied by the Instron machine are determined based on the ultimate failure force observed during the first run of each sample type. A margin of safety from the ultimate failure force is taken and then divided by 10 to obtain the force increments shown in Table 4.2. The

overall experimental procedures for each type of samples can be broken down and is summarized in Appendix A.

4.2.4 Data Collection for Inverse Problems

The experimental setup used in the inverse problem data collection is designed to be easily implemented. To neutralize the effect of gravity acting in the same direction as the displacement of the plate, the plate is clamped in a vertical fashion on a vice as shown in Figure 4.11. While at rest, an initial set of images are captured by cameras as reference for zero out-of-plane displacement shown on the left side of Figure 4.11. A non-zero displacement is then applied to the corner of the test specimen. After trial and error, displacing a small initial out-of-plane displacement at the corner of the plate with a finger is found to be the easiest method in providing an initial displacement without disturbing or changing the damping behavior of the plate as it oscillates back and forth. Once the corner is released, the cameras are triggered to capture the full field dynamic displacement of the plate. The image shown on the right of Figure 4.11 is an example of many images taken once the corner is released from an initial displacement.

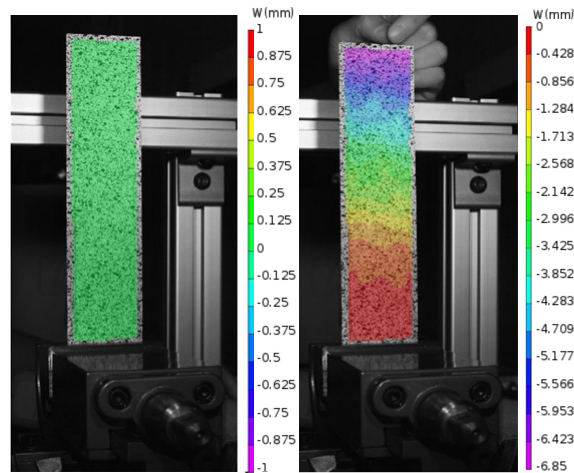


Figure 4.11: The left image shown is the initial image taken for zero displacement reference. The right image shown is the rest of the plate after it is released from an initial corner displacement.

Without a properly clamped boundary condition, Banks et al. explain in [35] that loss of energy can affect the overall structure and change the natural frequencies of the plates. To ensure the consistency of clamping condition at the cantilever boundary as shown in Figure 3.3 and Figure 4.11, a torque wrench is used with 49.05N-m to apply the same amount of clamping force on the aluminum and carbon fiber plates during data collections.

For inverse problem data collection, having accurate positions in both x and y coordinates while obtaining the full-field displacement is vital for matching information provided by the finite element code. To ensure the accuracy of x and y positions, axes markers for x and y directions are placed on the left bottom corner of test specimens as a reference for post-processing data. During out-of-plane displacement calculation in Vic-3D, coordinate transformation is first used to select the appropriate coordinate system. With the three point selection method shown in Figure 4.12 (origin, x axis, and y axis), the data processed will be adjusted to

have the desired orientations for x and y positions.

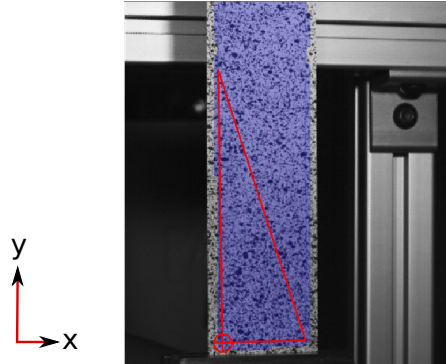


Figure 4.12: Example of coordinate transformation in Vic-3D to ensure accurate x and y position for inverse problem data. Coordinate transformation for x and y axes is performed by matching the axes marking on the test specimens.

One might notice in Figure 4.12, the coordinate system's origin is not exactly at the left bottom corner of the plate, as it should be for consistency with the finite element model shown in Figure 3.3. With known marker distance from the bottom and left edge of the plate set as 5mm, the x and y position obtained from Vic-3D can again be offset using MATLAB before the data is being used in the inverse problem.

The next section will describe the data collection procedures used in vibration analysis to obtain the FRFs of output vs. input displacement as well as verifying the resonance frequencies obtained for experimental and theoretical data.

4.2.5 Data Collection for Vibration Analysis

This section will explain the equipment and software used as well as experimental setup for vibration analysis data collection.

Mini SmartShaker Setup

To investigate the resonance frequency of the aluminum and carbon fiber test specimens, a shaker is used for vibration analysis. The shaker model is K2007E01 Mini SmartShaker from the Modal Shop Inc., with a power amplifier embedded into the shaker so that no external power amplifier is needed. At its maximum 1VAC RMS voltage input, the shaker can operate as high as 9kHz in frequency. However, the amplitude of the shaker reduces greatly with high frequencies. With frequency lower than 20Hz, the shaker can oscillate with a maximum amplitude around 8mm. With frequency as high as 200Hz, the frequency can only oscillate with a maximum amplitude of 0.4mm. To attach and vibrate the testing plate in a cantilever style similar to the inverse problem data collection, an aluminum fixture is custom made and speckled to serve as the connection between the shaker and the plate as well as the input displacement recorded. To isolate the shaker system, a frame structure is constructed to suspend the shaker and plate with strings in the direction perpendicular to the direction of vibration as shown in Figure 4.13. Although two identical plates are attached to the fixture on the shaker for balancing purpose, only one plate's image will be captured by the cameras for output displacement data along with input displacement from the fixture.

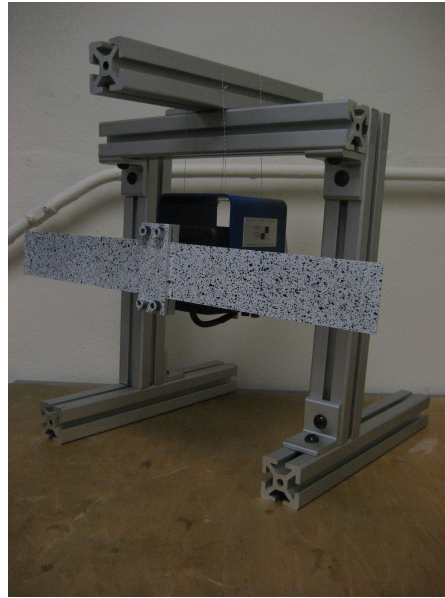


Figure 4.13: Setup with speckled plate and attachment with suspended fixture for vibration isolation.

LabVIEW SignalExpress

National Instrument's NI USB-4431 Compact DAQ with one analog output is used as the signal source for the shaker while LabVIEW SignalExpress software is used for setting up the input signal. SignalExpress allows the users to apply a sweeping sinusoidal wave as an excitation from the shaker, which we use as u_0 in Equation 3.19 is

$$u_0 = a \sin(\omega(t)t), \quad (4.1)$$

where $\omega(t)$ is the sweeping frequency that varies with time

$$\omega(t) = 100t. \quad (4.2)$$

Variable a in Equation 4.1 is the amplitude set at 500mV with an offset of 500mV for maximum amplitude applied. The sample rate is set at 51200 samples per

second with block size of 102400 samples. Having this setup with repeated signal activated, the shaker will sweep through frequency up to 200Hz every two seconds based on Equation 4.2. Similar to experiments discussed previously, the first set of images will be recorded while the shaker is stationary as reference images for zero out-of-plane displacement. With the high speed cameras synchronized at 400 frames per second capturing 999 frames, the dynamic behavior of the plate within the first couple modes can be fully recorded while the shaker sweeps through 200Hz in frequency. Three samples for each aluminum, 0° , and 15° carbon fiber plate will be tested to obtain the average FRFs.

5 RESULTS

In this chapter, the results obtained from various experiments discussed previously will be presented. A 95% confidence interval for the out-of-plane DIC displacement is calculated and first shown in Section 5.1 in comparison with a micrometer's displacement. To find the parameters such as Young's modulus and Poisson's ratio, Aluminum 6061 material has consistent known values and they can be obtained without any additional testing. However, the specific T800 uni-directional carbon fiber used in this project are not well tested. Tensile testing methods are performed to obtain the results presented in Section 5.2. Having known material parameters for both materials, the results obtained from the inverse problem approach are discussed in Section 5.3 and 5.4 for aluminum and carbon fiber plates respectively. The last two sections in this chapter cover the vibration analysis results obtained for both aluminum and carbon fiber plates to validate the parameters estimated by evaluating the theoretical and experimental resonance frequencies for the first two modes.

5.1 Error Analysis of Digital Image Correlation

To better understand the accuracy of DIC with current experimental setup, an ad hoc error analysis is done and Table 5.1 shows the comparison between known displacement measured from the micrometer and the calculated displacement processed by Vic-3D software. The Mitutoyo micrometer used has a smallest increment of 0.01mm, without other specification from the manufacturer of the micrometer, zero order uncertainty can be evaluated as half of the smallest increment,

which is 0.005mm. From the mean displacement and standard deviation shown in Table 5.1 for Vic-3D based on current experimental setup, the overall noise in the data collected by the cameras for out-of-plane displacement is less than 0.1mm.

Table 5.1: Comparison of displacement measured from a micrometer and calculated using Vic-3D.

Micrometer Displacement (mm)	Micrometer Stand Dev. (mm)	Vic-3D Displacement (mm)	Vic-3D Stand Dev. (mm)
0.5	0.005	0.5	0.07
1	0.005	1	0.08
1.5	0.005	1.53	0.09
2	0.005	2.04	0.08

The full field displacement data points are distributed normally and varied between 4534 to 4541 in number, with a plate size of 100cm² approximately. Using the T-distribution table provided in [36], the best estimate of x_i with a 95% confidence interval can be calculated and is shown in Table 5.1 with the equation

$$x_i = \bar{x} \pm 1.960S_x(95\%), \quad (5.1)$$

where x_i is the best estimate for x per set of data, \bar{x} is the mean value, and S_x is the standard deviation of the data. The value 1.960 shown in Equation 5.1 is the t-estimator found in T-distribution table for 95% confidence level [36]. Table 5.2 shows both the upper and lower bounds of the 95% confidence interval over four sets of data taken. The data sets shown in Table 5.1 are related to the micrometer displacements shown in Table 5.2.

Table 5.2: 95% confidence interval calculated using T-distribution.

Data Sets	Nominal Displacement (mm)	Number of Data Collected	Vic-3D Mean (mm)	Confidence Interval Lower Bound (mm)	Confidence Interval Upper Bound (mm)
1	0.5	4538	0.497	0.360	0.634
2	1	4534	1.004	0.847	1.161
3	1.5	4541	1.526	1.350	1.702
4	2	4534	2.044	1.887	2.201

With results shown in Table 5.1 and Table 5.2, the cameras and Vic-3D's noise and errors in data can be examined while evaluating data collected using DIC for rest of the experiments.

The next section will discuss the results obtained from tensile testing specifically for the carbon fiber material used. The aluminum 6061 used are well tested and the consistent values can easily be obtained without any additional testing.

5.2 Carbon Fiber Material Parameters from Tensile Testing

To obtain results for Young's modulus in both along and normal to the fiber orientation, the stress and strain of the data from tensile tests are needed. The stress applied to the test specimens is calculated based on

$$\sigma = \frac{F}{A}, \quad (5.2)$$

where F is the tensile force applied and recorded by the Instron machine, and A is the cross sectional area of the test specimen measured before they are speckled. Strain data is the ratio of elongation to its original length, which is collected separately with both extensometer as well as DIC for direction along the tensile force. Young's modulus E can be determined by linearly fitting the slope of the stress and strain curve and expressed as

$$E_i = \frac{\sigma_i}{\epsilon_i} \quad (i = 1, 2), \quad (5.3)$$

where $i = 1, 2$ are the principal directions shown in Figure 3.2. Young's modulus in the first direction E_1 can be measured and calculated by performing tensile tests using 0° specimens, while Young's modulus in the second principal axis E_2 can be found utilizing 90° carbon fiber test specimens. Although both extensometer and DIC are capable of finding the strain along the tensile direction as well as the Young's moduli, only DIC is capable in recording the strain perpendicular to the tensile direction at the same time. To calculate the Poisson's ratio

$$\nu = -\frac{\epsilon_{transverse}}{\epsilon_{axial}}, \quad (5.4)$$

strain value in both axial and transverse directions are required. Similar to Young's modulus, Poisson's ratios in both principal directions can be obtained by testing 0° and 90° carbon fiber test samples. However, for 90° carbon fiber samples, the strain values found in the transverse direction are so small, they have the same magnitude for their mean values and standard deviations. Since the mean values for strain cannot be distinguished from noise, the Poisson ratio for 90° carbon fiber

samples are calculated using the following equation

$$\nu_1 = E_1 \frac{\nu_2}{E_2}. \quad (5.5)$$

Shear modulus G discussed previously and shown in Equation 3.9 is analogous to Young's modulus E such that it is the constant ratio between shear stress σ_{12} and shear strain ϵ_{12} in the elastic region. With the $\theta = 10^\circ$ off angle test specimens, the shear stress can be calculated:

$$\sigma_{12} = \frac{1}{2}\sigma_y \sin(2\theta) = 0.171\sigma_y. \quad (5.6)$$

With coordinate system shown in Figure 3.2, the shear stress is calculated by Vic-3D based on images collected performing the tensile test with 10° off-angle test specimens. Table 5.3 shows results of Young's modulus, Poisson's ratio, and shear modulus obtained from extensometer and DIC data.

Table 5.3: Parameter results obtained from extensometer and digital image correlation for Young's modulus, Poisson's ratio, and shear modulus.

	Fiber Orientation	Methods	Sample 1	Sample 2	Sample 3	Sample 4
Young's Modulus (GPa)	90°	extens	N/A	8.13	7.76	8.05
		DIC	N/A	6.15	6.4	6.31
	0°	extens	N/A	145.5	147.4	154.9
		DIC	144.2	148.7	146.9	157
Poisson's Ratio	90°	calculated	N/A	0.0156	0.0163	0.0172
	0°	DIC	0.321	0.378	0.374	0.427
Shear Modulus (GPa)	10°	DIC	N/A	11.2	9.35	9.04
	Fiber Orientation	Methods	Sample 5	Sample 6	Average	Stdv
Young's Modulus (GPa)	90°	extens	7.72	N/A	7.91	0.21
		DIC	6.85	N/A	6.29	0.13
	0°	extens	159.9	N/A	151.96	6.72
		DIC	155.8	N/A	149.2	5.52
Poisson's Ratio	90°	calculated	0.0171	N/A	0.0166	0.0008
	0°	DIC	0.39	N/A	0.375	0.04
Shear Modulus (GPa)	10°	DIC	8.25	10.95	9.86	1.17

As mentioned in the test procedure section, sample 1 is often used for mock-up experiment and hence incomplete data collected. For finding Young's modulus and Poisson's ratio, only 5 samples are used which explains the void for sample 6 data shown. The average and standard deviation of the material parameters are also calculated and shown in Table 5.3. The values for Young's modulus obtained from extensometer and DIC are overlapped and well correlated within the standard deviation value for 0° orientation. For 90° test specimens, the Young's modulus found with two separate methods are reasonably close within 1.5GPa yet they are not overlapped. The parameters found in Table 5.3 can be used as reference or comparison for results found in the inverse problem and vibration analysis.

5.3 Inverse Problems for Aluminum Plates

During parameter estimation, a surface fit is used for smoothing the displacement data while a second order difference scheme is used for calculating the velocity. Figure 5.1 shows the displacement for the center of the plate at node 3,13 from finite element estimation in red and data collected from DIC in blue based on the material parameters estimated. The Young's modulus E is estimated to be 67.89GPa, the air-resistance damping parameter α is 1.198, and the Kelvin-Voigt damping parameter β is 1.002×10^{-5} as shown in Figure 5.2. The residual is shown in Figure 5.3 such that in the first 20 iterations, the residual quickly decreases and stays around 0.96×10^{-5} m as the iteration continues fine tuning in parameter estimation. The Young's modulus E estimated is consistent with the known Young's modulus value of 68.9GPa for 6061 aluminum. To evaluate the damping parameters found, vibration analysis results can be used to compare the resonance frequency for the first two modes using the parameters estimated and the experimental data.

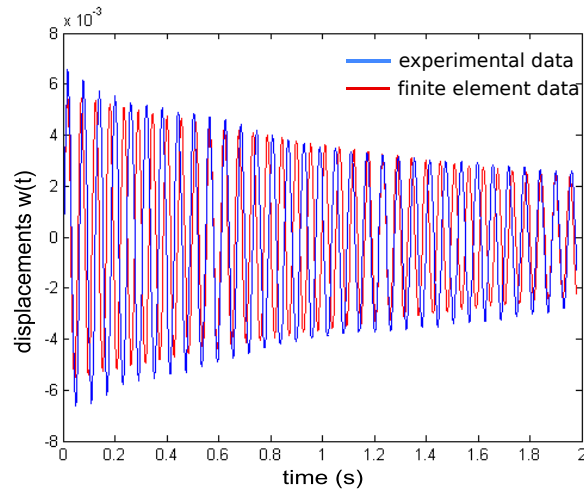


Figure 5.1: Displacement matching results for the center of aluminum plate between finite element model and experimental data collected from DIC. The finite element data in red matches the Experimental data displayed in blue well such that the plots' amplitudes and frequency are consistent.

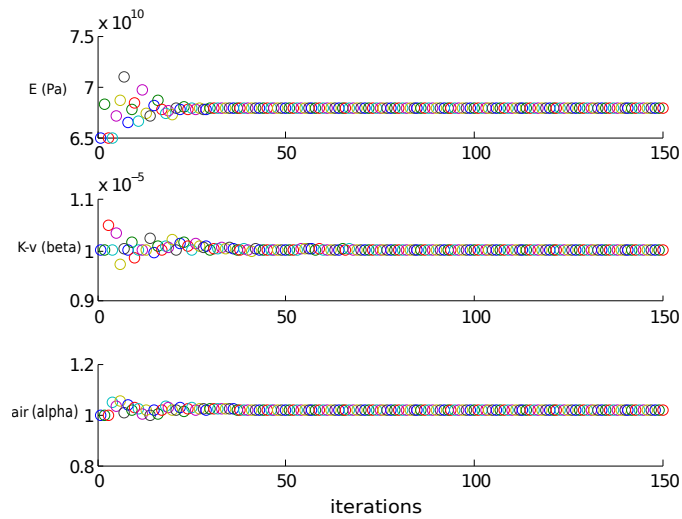


Figure 5.2: Material parameter estimation for 6061 aluminum plate for Young's modulus and the two damping parameters for each iteration calculated by the inverse problems. Each color circle is the material parameter calculated during each iteration in the inverse problem.

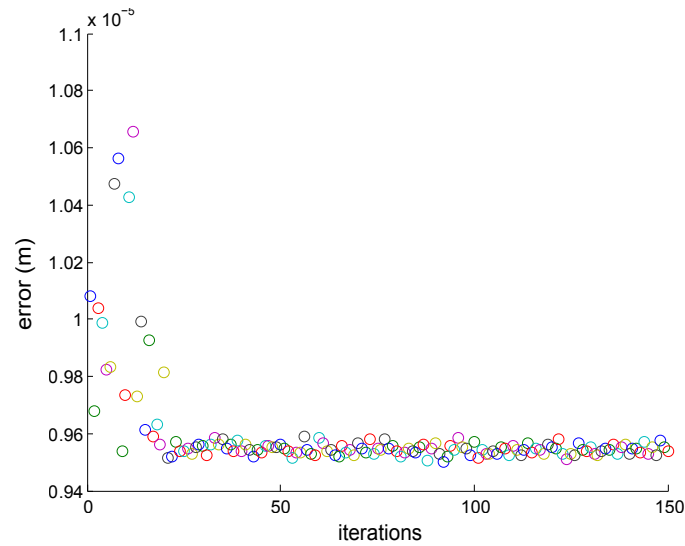


Figure 5.3: Residual of full field displacement between experimental data and finite element prediction. Each color circle is the error calculated between the two sets of data during each iteration in the inverse problem.

The theoretical model used for finite element assumes the the plate to oscillate evenly in amplitude and its average displacement should be zero. Due to noise in data collection, the experimental data shown in blue is not oscillating perfectly about zero displacement and has an offset of 0.2mm shown in blue in Figure 5.1, which may have some effect on the results of material parameter estimated. The offset is calculated by averaging over the entire experimental data set. However, as seen in Figure 5.1, the displacement results produced from the finite element code with the material parameters estimated are able to match the experimental data reasonably. Although Nelder-Mead method used in the inverse problem estimating algorithm can be simply implemented with noisy data, the simplex searching method is computationally expensive, which for good estimation results, accurate initial guesses are essential. With material parameters well estimated, the inverse problem can be used as a validation for the finite element code in modeling

aluminum plates.

5.4 Inverse Problems for Carbon Fiber Plates

In contrast to aluminum material parameter estimation, the inverse problem results found in both 0° and 15° carbon fiber plates are unsuccessful. The inverse problem is not able to make any steps with the displacement produced by the finite element code, which produces displacement that is not in the proximity of the experimental displacement data. To salvage this problem, the material parameters found in tensile testing such as Young's moduli E_1 and E_2 are used in the inverse problem as initial guesses. An example of the displacement result is shown in Figure 5.4.

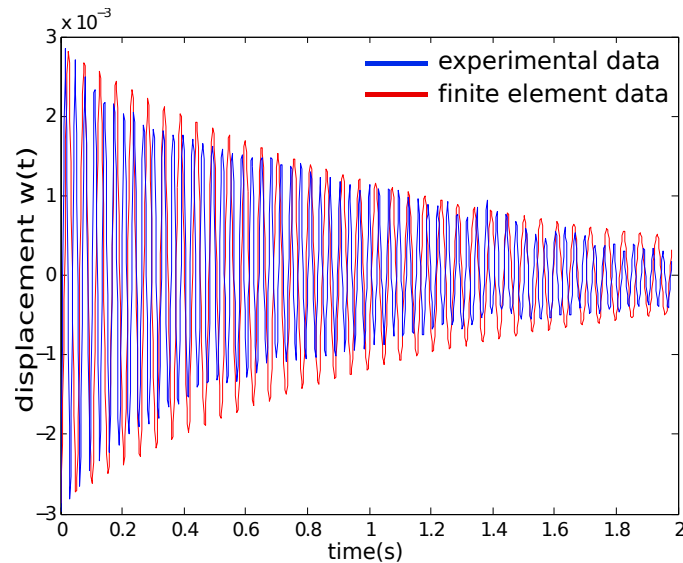


Figure 5.4: An example of inconsistent displacement matching results between finite element model and experimental data collected from DIC. Experimental data is displayed in blue, while finite element result is displayed in red. Although the amplitude displayed by the finite element might seem reasonable in comparison with the data from DIC in blue, the frequency mismatch between the blue and red displacements shows an inconsistency with approximately multiple of two.

Even with this approach, the inverse problem is still not able to properly match the displacement between the finite element code and the experimental data. As seen in 5.4, although the amplitude of the finite element displacement seems to somewhat follow the experimental data in blue, upon close inspection, the frequency between the two results are not consistent. With successful inverse problem results obtained from testing the aluminum plates, thin-plate finite element model used based on Kirchhoff-Love plate theory with the damping assumption might not be suitable for carbon fiber materials. To further examine this problem, the vibration analysis will be used with known material parameters from the tensile test to investigate the resonance frequency using the same finite element model and compare with results found in shaker testing.

5.5 Vibration Analysis of Aluminum Plates

As discussed in Chapter 3, using Equations 3.26 and 3.29 the material parameters can be inserted back to the finite element model used to determine resonance frequencies of the first couple modes. With the material parameters for the aluminum plate obtained from the inverse problem, the first two resonance frequencies are 17.57Hz and 109.87Hz, based on the finite element model. Once the input and output displacements from the shaker test are obtained using DIC, the FRF using Fast Fourier Transform of the input and output displacements can be plotted in the frequency domain. Three test samples are tested on the shaker, and the FRFs are shown in Figure 5.5. For all three aluminum plates, the FRFs are quite consistent in terms of displaying the resonance frequencies of the first two modes which are the peaks displayed in Figure 5.5. Resonance frequency peak is calculated

when there is greatest ratio between output displacement reacted based on input displacement excitation. The advantage of using FRF for vibration analysis is that the data can be averaged easily within the frequency domain and potentially reduce the noise in the data. The average FRF for the aluminum plates is shown in Figure 5.6. The resonance frequency of the first two modes of the aluminum plates are found to be 17.18Hz and 101.2Hz, which again validates the accuracy of finite element code in modeling the aluminum plates.

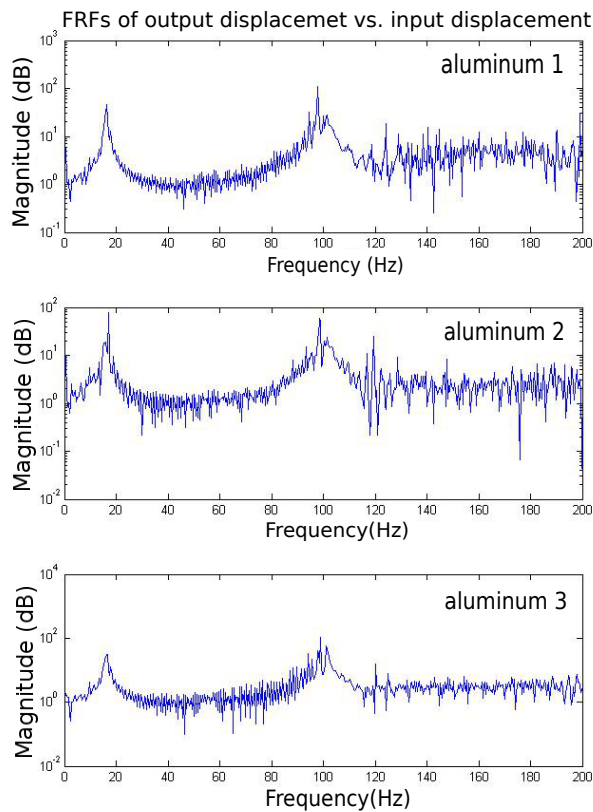


Figure 5.5: FRFs of input and output displacement of the three aluminum testing samples. Resonance frequencies are peaks shown in the plot such that the output displacements are the greatest with respect to given input displacements.

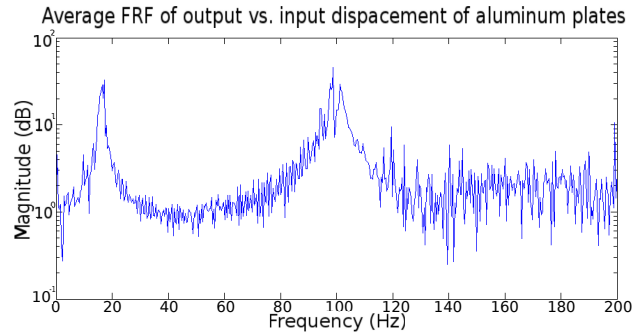


Figure 5.6: Average FRF of input and output displacement of the three aluminum testing samples. The resonance frequencies of the first two modes found in the shaker test are 17.18Hz and 101.2Hz.

5.6 Vibration Analysis of Carbon Fiber Plates

Although the inverse problem results are not successful in estimating the Young's moduli E_1 and E_2 , and the angle ply direction, the results found from the vibration test with the shaker can be used to validate that the finite element model might not represent the uni-directional carbon fiber material well. Instead of using the material parameters estimated from the inverse problem, the material parameters found from the tensile tests will be used for comparison. After inputting the material parameters tested into the finite element code and calculating the frequencies, the 0° uni-directional carbon fiber plates are supposed to resonate at 19.64Hz and 117.85Hz for the first two modes based on the theoretical data. However, the results shown from averaging the three samples of carbon fiber plates shown in Figure 5.7 and Figure 5.8, frequencies for the first two modes should be at 32.8Hz and 99.5Hz.

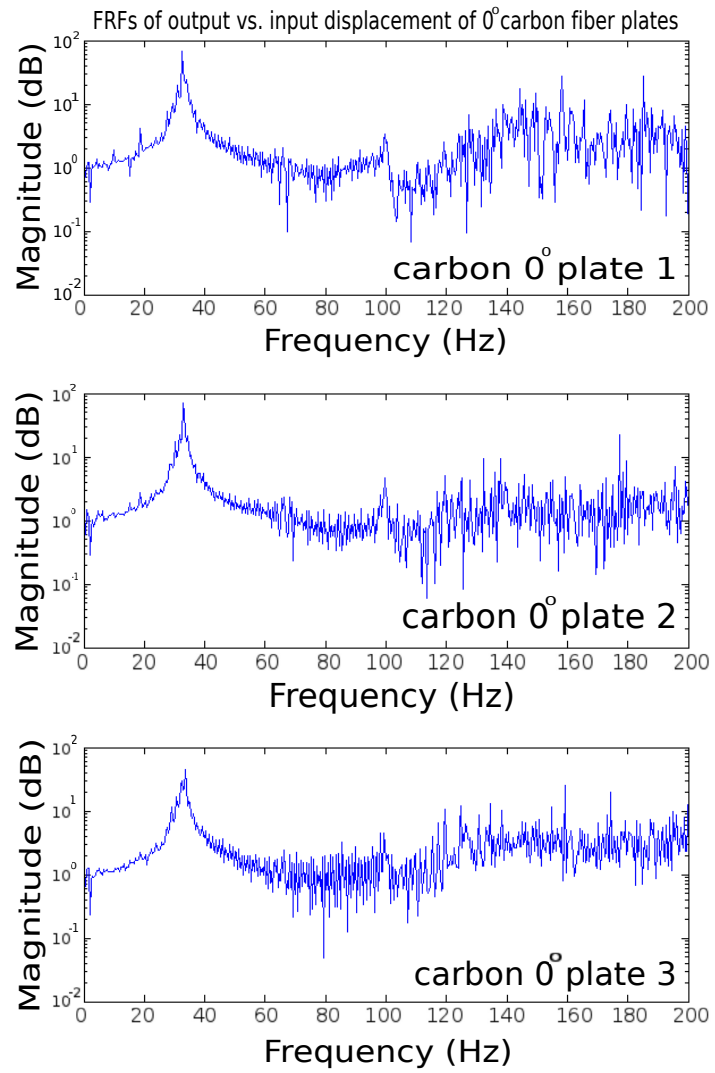


Figure 5.7: FRFs of the three carbon fiber samples with zero degree angle. All three carbon fiber samples seem to produce consistent FRFs qualitatively.

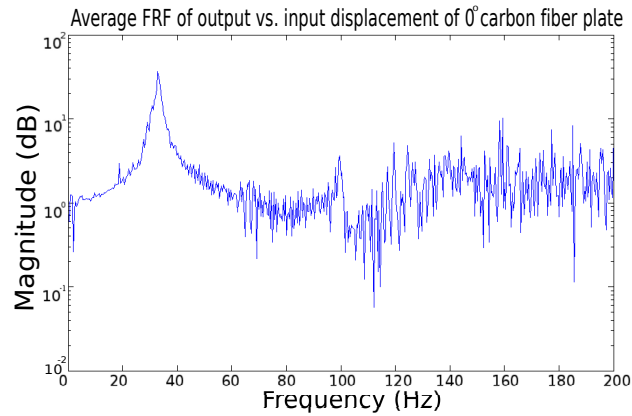


Figure 5.8: Average FRF of output vs. input displacement of carbon fiber samples with zero degree angle.

Aside from learning that the finite element code can misrepresent the uni-directional carbon fiber material, one can see the second resonance frequency of 99.5Hz shown in Figure 5.8 is not as visible and clear compared to the first mode at 32.8Hz. This is due to the fact that the second frequency exhibits in a twisting motion, such that it is difficult to detect for a supposed well balanced 0° ply layout with very low stiffness along the width of the plate.

Using the same procedures, the known material parameters of the 15° carbon fiber plates from the tensile tests are entered into the finite element model to calculate the first two resonance frequencies. The theoretical results from the finite element mode for the first two modes are found to be 10.6Hz and 66.86Hz. The results obtained from averaging three samples of 15° carbon fiber plate from Figure 5.9 are shown in Figure 5.10. By extracting the frequency values from the highest peaks in Figure 5.10, 16.8Hz and 100Hz are found to be the first two resonance frequencies. The theoretical resonance frequencies of the 15° plates for the first two modes are substantially lower than the frequencies measured from the shaker test using DIC, which presents similar challenges discussed previously for

the 0° carbon fiber plates.

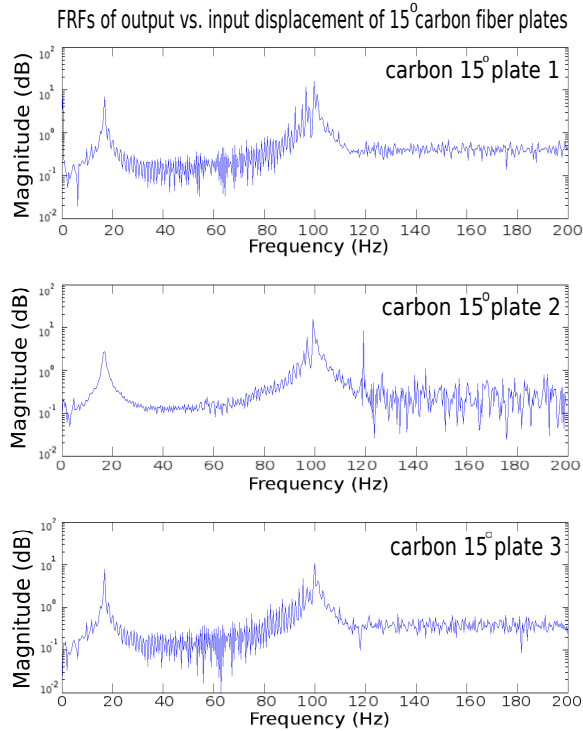


Figure 5.9: Three FRFs of output vs. input displacement of the carbon fiber samples with 15 degree angle.

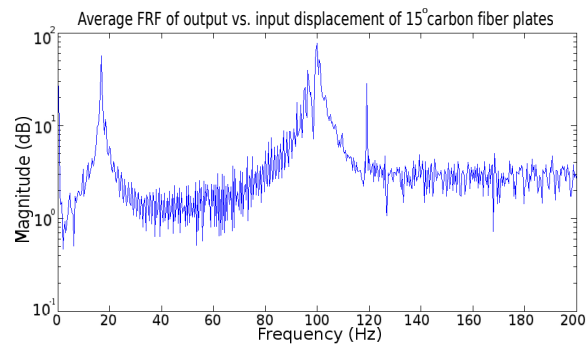


Figure 5.10: Average FRF of output vs. input displacement of the three carbon fiber samples with 15 degree angle.

With 15° off angle, the carbon fiber plate is no longer balanced during the

shaker test and it exhibits a curling or twisting motion similar to Figure 5.11, which results in a very pronounced second resonance frequency at 100Hz. Also, since the stiffness along the span of the plate is reduced compared to the 0° carbon fiber test specimen, the first resonance frequency for the 15° off angle plate shown in Figure 5.10 is less than the 0° carbon fiber plate observed in Figure 5.8.

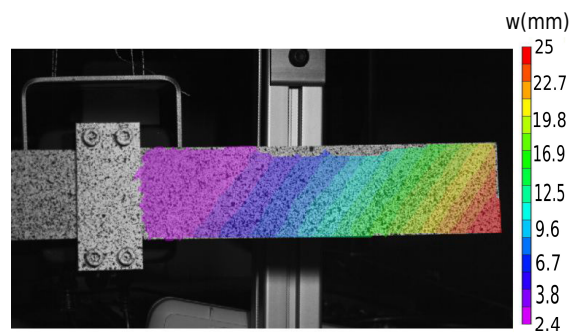


Figure 5.11: An example of the 15 degree carbon fiber plate exhibiting the second mode shape in twisting during shaker test. This image has been post processed by DIC. Notice the right bottom corner is curling out of plane and has the greatest displacement around 25mm while the base excites with displacement around 2mm.

6 CONCLUSIONS AND FUTURE WORK

The purpose of this project is to propose and implement a new testing method with digital image correlation in vibration analysis as well as characterizing the material parameters of carbon fiber and aluminum plates. Nelder-Mead algorithm is used within the inverse problem to minimize the results in dynamic behavior from finite element model and experimental data. Three types of test samples are made and tested: 6061 aluminum plates, 0° carbon fiber plates, and 15° carbon fiber plates. Overall the project successfully utilized DIC in collecting all experimental data.

Experimental data of the full-field displacement are collected for all test specimens. A stationary vice is used to provide a cantilever boundary condition and the plates are released from an initial corner displacement. The results of the dynamic displacements of the plates recorded by DIC are used for the inverse problem. Shaker tests are also done on all test specimens as a validation for the material parameters obtained from the inverse problem as well as a validation of the accuracy of the finite element model for aluminum and uni-directional carbon fiber. Along with two types of experiments explained, the traditional tensile testing with DIC is also carried out on the carbon fiber material for obtaining the material parameters while the aluminum material parameters has been well tested with known parameters prior to this project. Fabrication and testing methods are explained in detail for future validation or expansion of current experiments.

As an initial attempt in material characterization using DIC, the material parameter results for aluminum plates are consistent with the known material parameters for aluminum 6061. The vibration analysis also further validates the material parameters and the finite element code in matching the experimental and theoret-

ical resonance frequencies for the first two modes. However, in investigating the material parameters for the 0° and 15° carbon fiber plates, the inverse problem is not able to estimate the material parameters. In addition, even with known results found from the tensile tests, the finite element model cannot accurately represent the dynamic behavior of either type of carbon fiber test specimens during vibration analysis. The results of this project validate that the Kirchoff-Love thin plate theory in the finite element model, should only be used in estimating isotropic material parameters or quasi-isotropic of composite laminates. Also, the assumptions made in proportional damping will need to be modified and improved to model the carbon fiber plates reasonably. Despite having difficulties in estimating the carbon fiber material parameters, the results found in the vibration analysis is consistent with the prediction of plates' dynamic behavior based on their stiffness and layup angles. In terms of experimental data collection, DIC has proven to be reliable in measuring full field displacement data and also capturing modal frequencies in vibration analysis.

For future material characterization of carbon fiber using the inverse problem approach, greater attention in modeling damping might alleviate the challenges faced within this project, as well as using quasi-isotropic or less non-isotropic laminates for validation. Other plate models may be used for predicting the material parameters as well. In particular, additional parameters associated with nonlinear terms might be implemented for more accurate model estimation since this project only utilized a linear plate model. As for vibration analysis, having Equation 3.24 that represents the theoretical FRF of output vs. input displacement, an iterative process similar to an optimization or inverse problem approach can be used in determining the damping parameters. The results found from the vibration analysis

can then be used as comparison for accuracy of the inverse problem approach. This project has utilized DIC in full field displacement data collection as well as modal frequencies in vibration analysis. Further development in obtaining mode shapes with modal frequencies can help better understand the characteristics of composite structures.

APPENDICES

A EXPERIMENTAL PROCEDURES IN TENSILE TESTING

1. Measure, calculate, and record the cross section area of the test samples.
2. Speckle the samples with aerosol spray paint.
3. Setup, calibrate, and synchronize the cameras.
4. Secure the top side of the first sample with top Instron's grip.
5. Zero and balance the load applied by the Instron machine.
6. Secure the bottom side of the first sample with bottom Instron's grip.
7. Start the tensile test on the Instron machine.
8. With approximated ultimate tensile strength obtained from the first tensile test, determine the removal force of extensometer as well as multi-buffering settings on cameras based on Table 4.2.
9. Repeat step 2 through step 6 for the rest of the samples.
10. Adjust the travel of the Instron machine to as close to zero load as possible.
11. Attach extensometer on the test specimen.
12. Zero and balance the strain on the extensometer.
13. Take initial set of images with cameras.
14. Start the tensile test on the Instron machine.
15. Trigger cameras with increments based on Table 4.2.

16. Remove extensometer when prompt by the Instron machine.
17. Continue the tensile test and image capturing.
18. Download all sequences of images from cameras based on Figure 4.7

BIBLIOGRAPHY

- [1] M. Grediac. The use of full-field measurement methods in composite material characterization: Interest and limitations. *Composites: Applied Science and Manufacturing*, 35:751–761, 2004.
- [2] N. McCormick and J. Lord. Digital image correlation. *Materials Today*, 13(12):52–54, December 2010.
- [3] J.W. Dally and W.F. Riley. *Experimental Stress Analysis*. College House Enterprises LLC, 4 edition, 2005.
- [4] M.A. Sutton, W.J. Wolters, W.H. Peters, W.F. Ranson, and S.R. McNeill. Determination of displacements using an improved digital correlation method. *Image and Vision Computing*, 1:133–139, 1983.
- [5] L.C.S. Nunes, D.A. Castello, P.A.M. dos Santos, and C.F.T. Matt. Identification of material properties using full-field and non contact measurements. *Journal of the Brazilian Society of Mechanical Science and Engineering*, 31:167–172, 2009.
- [6] B. Pan. Recent progress in digital image correlation. *Experimental Mechanics*, 51:1223–1235, 2011.
- [7] C. Niezrecki, P. Avitabile, C. Warren, P. Pingle, and M. Helfrick. A review of digital image correlation applied to structural dynamics. In E.P. Tomasini, editor, *9th International Conference on Vibration Measurements by Laser and Noncontact Techniques and Short Course*, volume 1253, pages 219–232. International Conference on Vibration Measurements by Laser and Noncontact Techniques and Short Course, 2010.
- [8] *Application of High Speed Digital Image Correlation for Measurement of Mode Shapes Analysis*, Indiana USA, June 2010. the SEM Annual Conference.
- [9] T. Siebert, R. Wood, and K. Splitthof. High speed image correlation for vibration analysis. *Journal of Physics*, 181(012064), 2009.
- [10] L.C.S. Nunes, D.A. Castello, C.F. Matt, and P.A.M. dos Santos. Parameter estimation using digital image correlation and inverse problems. *Mechanics of Solids in Brazil*, 1:433–443, 2007.
- [11] J.C. Dupre, M. Bornert, L. Robert, and B. Wattrisse. Digital image correlation: displacement accuracy estimation. *EPJ Web of Conferences*, 6:31006:1–8, 2010.

- [12] H. Haddadi and S. Belhabib. Use of rigid-body motion for the investigation and estimation for the measurement errors related to digital image correlation technique. *Optics and Lasers in Engineering*, 46:185–196, 2008.
- [13] T. Siebert, T. Becker, K. Spiltthof, I. Neumann, and R. Krupka. High-speed digital image correlation: error estimations and applications. *Optical Engineering*, 46(5):051004:1–7, 2007.
- [14] R.C. Aster. *Parameter Estimation and Inverse Problems*. Elsevier Academic Press, Boston, 2005.
- [15] J.V. Beck and K.J. Arnold. *Parameter Estimation in Engineering and Science*. Wiley, New York, 1977.
- [16] J.V. Beck and K.A. Woodbury. Inverse problems and parameter estimation: integration of measurements and analysis. *Measurement Science and Technology*, 9:839–847, 1998.
- [17] M.N. Ozisik and H.R.B. Orlande. *Inverse Heat Transfer: Fundamentals and Applications*. Taylor and Francis, New York, 2000.
- [18] S. Cooreman, D. Lecompte, H. Sol, J. Vantomme, and D. Debruyne. Identification of mechanical material behavior through inverse modeling and dic. *Experimental Mechanics*, 48:421–433, 2008.
- [19] J.C. Lagarias, J.A. Reeds, and M.H. Wright. Convergence properties of the nelder-mead simplex method in low dimensions. *SIAM Journal of Optimization*, 9(1):112–147, 1998.
- [20] T.G. Kolda, R.M Lewis, and V. Torczon. Optimization by direction search: New perspective on some classical and modern method. *SIAM Review*, 45(3):385–482, 2003.
- [21] R. Chandra, S.P. Singh, and K. Gupta. Damping studies in fiber-reinforced composite - a review. *Composite Structures*, 46:41–51, 1999.
- [22] R.D. Adams and D.G.C. Bacon. Effect of fibre orientation and laminate geometry on the dynamic properties of cfrp. *Journal of Composite Materials*, 7:402–408, 1973.
- [23] R.D. Adams and M.R. Maheri. Dynamic flexural properties of anisotropic fibrous composite beams. *Composites Science and Technology*, 50:497–514, 1994.
- [24] J. He and Z.F. Fu. *Modal Analysis*. Butterworth-Heinemann, 2001.
- [25] C.W. de Silva. *Vibration, Fundamentals and Practice*. CRC Press LLC, 1999.

- [26] IEEE Solid-State Sensor and Actuator Workshop. *A Comparison of Fixed-Base and Driven-Base Modal Testing of an Electronic Package*, Hilton Head Island, SC, USA, 1992.
- [27] O.B. Ozdoganlar, B.D. Hansche, and T.G. Carne. Experimental modal analysis for microelectromechanical systems. *Experimental Mechanics*, 45(6):498–506, 2005.
- [28] F.R. Vigneron and Y. Soucy. Driven-base tests for modal parameter estimation. *AIAA*, 25(1):152–160, October 1985.
- [29] P. L. Gatti and V. Ferrari. *Applied Structural and Mechanical Vibrations*. E & FN Spon, 1999.
- [30] J.N. Reddy. *Theory and Analysis of Elastic Plates and Shells*. CRC Press LLC, 2007.
- [31] R.D. Adams, M.A.O. Fox, R.J.L. Flood, R.J. Friend, and R.L. Hewitt. The dynamic properties of unidirectional carbon and glass fiber reinforced plastics in torsion and flexure. *Journal of Composite Materials*, 3:594–603, 1969.
- [32] I.M. Daniel and O. Ishai. *Engineering Mechanics of Composite Materials*. Oxford University Press, New York, 2006.
- [33] ASTM Standards D3039/D3039M. *Standard Test Method for Tensile Properties of Polymer Matrix Composite Materials*. ASTM International, 100 Barr Harbor Drive, PO Box C700, West Conshohocken, PA, 2009.
- [34] C.C. Chamis and J.H. Sinclair. Ten-deg off-axis test for shear properties in fiber composites. *Experimental Mechanics*, 17(9):339–346, 1977.
- [35] H.T. Banks, R.C. Smith, and Y. Wang. Modeling and parameter estimation for an imperfectly clamped plate. In *Progress in Systems and Control Theory*, volume 20, pages 23–42, 1995.
- [36] R.S. Figliola and D.E. Beasley. *Theory and Design for Mechanical Measurements*. John Wiley and Sons, Inc, 2006.